

First-principles study of Rh- and Pd-based kagome-layered shandites

Luca Buiarelli,^{1,2} Turan Birol,² Brian M. Andersen,¹ and Morten H. Christensen^{1,*}

¹*Niels Bohr Institute, University of Copenhagen, 2200 Copenhagen, Denmark*

²*Department of Chemical Engineering and Materials Science, University of Minnesota, MN 55455, USA*

(Dated: August 1, 2025)

The shandite structure hosts transition metals arranged in kagome layers stacked rhombohedrally, and interspersed with post-transition metal ions and chalcogens. The electronic states near the Fermi level are dominated by the transition metal *d*-orbitals and feature saddle points near several of the high-symmetry positions of the Brillouin zone, most notably the F and L points. Combining symmetry considerations with *ab initio* methods, we study the electronic and structural properties of these materials with an emphasis on the connection between electronic saddle points at specific momenta and structural instabilities at these momenta. While the parent compounds studied are all found to be structurally stable in the $R\bar{3}m$ space group under ambient conditions we show that, in specific compounds, moving the saddle point closer to the Fermi level using either hydrostatic pressure or doping, can induce a structural instability. The importance of the electronic degrees of freedom in driving this instability is supported by the dependence of the frequency of the soft phonon mode on the electronic smearing temperature, as is the case in charge density wave materials. Our first-principles calculations show that as the smearing temperature is increased, the compound becomes structurally stable again. Our findings survey the structural properties of a large family of shandite materials and shed light on the role played by saddle points in the electronic structure in driving structural instabilities in rhombohedrally stacked kagome-layered materials belonging to the $R\bar{3}m$ space group.

I. INTRODUCTION

Kagome-layered materials have attracted a great deal of attention in the condensed matter physics and materials science communities recently [1, 2]. This increased interest has been engendered, in part, by the discovery of a giant anomalous Hall effect in $\text{Co}_3\text{Sn}_2\text{S}_2$ [3], superconductivity in the alkali-based AV_3Sb_5 kagome metals [4–6], and exotic charge orders in ScV_6Sn_6 [7] and FeGe [8]. Such a wide range of materials provide a fertile ground for studying the interplay between electronic correlations and lattice geometry. In particular, many of these compounds exhibit temperature-driven structural transitions accompanied by some type of charge order [7–14]. This raises the question of the relative role of the phononic and electronic degrees of freedom in driving these transitions: The electronic structure of the kagome lattice features van Hove points at multiple high-symmetry points of the Brillouin zone which promote the effects of correlations [15, 16]. In spite of this, the different materials exhibit distinct behaviors and the role played by electrons in driving the observed instabilities remains an open question.

In the AV_3Sb_5 materials, angle-resolved photo-emission spectroscopy (ARPES) measurements and density-functional theory (DFT) are in overall agreement [4, 17–19]. Both show an electronic structure with multiple van Hove points near the M point of the Brillouin zone [17, 20]. These are of both ‘pure’ and ‘mixed’ types, denoting the localization of the electronic wavefunction within one unit cell; at pure van Hove points, the

wavefunction is localized on a single atom of the kagome lattice, while at mixed van Hove points, it is localized on two of the kagome atoms [17, 21]. The pure versus mixed nature of the Bloch wavefunction has important consequences for the leading instabilities and the nature of the resulting ordered state [16, 22–31]. Charge order onsets near 100 K in all three AV_3Sb_5 compounds with a concomitant breaking of the translational symmetry and enlargement of the unit cell along the *a*-, *b*-, and *c*-directions [13, 32, 33]. There are indications that the charge order breaks time-reversal symmetry [10, 12, 34–38], although these observations remain controversial due to conflicting reports [39–41]. It is tempting to associate the charge order with an electronic instability driven by nesting of the large densities of states at the van Hove points [42–44]. However, the three-dimensional nature of the materials implies that van Hove points are associated with kinks in the density of states – rather than true divergences as in the two-dimensional case [15] – matching observations of at most a moderate increase in the density of states at the van Hove points [45]. Instead, the instability appears to be a consequence of the interplay between electronic and phononic degrees of freedom and it is absent if the two systems are decoupled [20, 44, 46–48]. Indeed, even the anharmonic couplings between phonon modes turn out to be important in stabilizing the charge density wave phase [49]. Charge order in FeGe emerges deep within an antiferromagnetic phase [8]. Similar to AV_3Sb_5 , ARPES finds multiple van Hove points near the Fermi level [14], and the ordering vectors of the charge order are the same in both FeGe and AV_3Sb_5 [8, 50]. However, the ARPES results are not faithfully reproduced by DFT calculations [14], indicating that correlations in FeGe play a prominent role in shaping the elec-

* mchriste@nbi.ku.dk

tronic structure, and might also drive the formation of a charge-ordered phase [51, 52]. The role of the van Hove points in shaping the physics of both AV_3Sb_5 and FeGe is in stark contrast to the phenomenology observed in ScV_6Sn_6 [7]. In this case, the charge order leads to a $\sqrt{3} \times \sqrt{3}$ enlargement of the unit cell driven by lattice fluctuations [53, 54]. This dichotomy raises the question of the role played by saddle points in the electronic band structure in shaping the interplay between electronic and structural degrees of freedom.

Here we explore the electronic structures of a large family of non-magnetic shandite compounds with the goal of mapping out the character of the van Hove points near the Fermi level and their potential role in driving the systems towards a structural instability. Shandites – or half-antiperovskites [55] – constitute a diverse family of compounds with chemical composition $M_3A_2Ch_2$, where M is a transition metal (Co, Ni, Rh, or Pd), A is a post-transition metal (In, Sn, Tl, Tb, or Bi) while Ch denotes one of the chalcogenides, S or Se. The most famous member of the shandites is the ferromagnetic $Co_3Sn_2S_2$ [56] which features a host of exotic phenomena from giant anomalous Hall [3, 57] and Nernst [58] effects to emergent Weyl fermions [59, 60] and enhanced magneto-optical responses [61]. Magnetism can be continuously suppressed by substituting Sn for In [62, 63] or Co by Ni [64] and magnetic shandites are, to the best of our knowledge, still rare. More recently, the nonmagnetic compound $Ni_3In_2S_2$ has been shown to feature a large magnetoresistance induced by Dirac nodal lines in the electronic structure [65]. On the other hand, shandite compounds based on Rh or Pd remain largely unexplored, and here we aim to bridge this gap.

The paper is organized as follows: In Sec. II we review the geometry of the shandite crystal structure and in Sec. III we present a phenomenological study of the structural instabilities possible in the shandites. The results of our first-principles calculations are presented in Sec. IV which also includes a study of the symmetry properties of the electronic bands. In Secs. IV A and IV B, we present detailed *ab initio* calculations of the effects of pressure and doping on specific shandite compounds. In Sec. V, we present our conclusions and discuss possible directions for future research.

II. SHANDITE CRYSTAL STRUCTURE

Shandites are rhombohedral materials that crystallize in the $R\bar{3}m$ space group (#166) with point group D_{3d} . This group permits perfect (i.e., non-distorted) kagome layers due to the presence of the three-fold roto-inversion symmetry $\bar{3}$, which is equivalent to a 60° rotation followed by a mirror in the plane perpendicular to the rotation axis. Such a kagome-layered structure is familiar from other materials, such as the quantum spin liquid candidate material herbertsmithite [66] or the frustrated magnet $Na_2Ti_3Cl_8$ [67, 68]. The crystal struc-

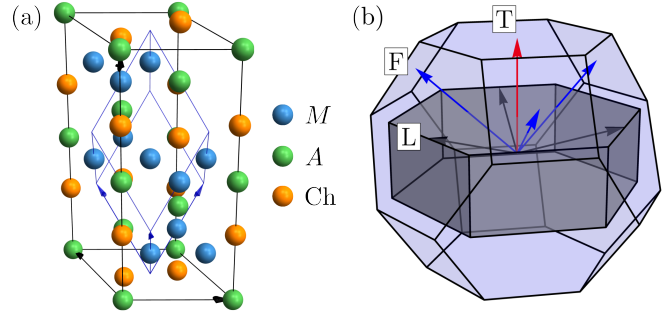


FIG. 1. (a) Schematic crystal structure of the shandite compounds. The rhombohedral primitive unit cell is denoted by the light blue arrows, while the hexagonal conventional cell is outlined in black. The kagome layers consist of the transition-metal ions, M , in deep blue. The post transition-metal ions, A , are green while the chalcogen ions, Ch , are orange. (b) First Brillouin zone for the space group $R\bar{3}m$. The Brillouin zone of the primitive unit cell is denoted in light blue, while the dark gray denotes the Brillouin zone of the conventional cell. The relevant high-symmetry points are highlighted by blue (F), black (L), and red (T) arrows, respectively. The stars of F and L contain three points while there is only a single point in the star of T.

ture contains three symmetry-equivalent kagome layers in the conventional hexagonal unit cell stacked in an ‘ABCABC...’ fashion. This is in contrast to simpler cases such as the alkali-based kagome metals AV_3Sb_5 in space group $P6/mmm$ and point group D_{6h} , in which a proper six-fold symmetry is present and the unit cell contains a single kagome layer (so the layers are stacked in ‘AAA...’ fashion). As a result, the crystal structure of the shandite materials is more involved than that of the corresponding hexagonal $P6/mmm$ kagome compounds, as shown in Fig. 1(a). However, a rhombohedral *primitive* cell can be constructed that only contains one kagome layer, outlined by the blue cell in Fig. 1(a). In terms of the conventional lattice parameters, the primitive translations are

$$\begin{aligned}\mathbf{R}_1 &= \frac{1}{3}(0, \sqrt{3}a, c), \\ \mathbf{R}_2 &= \frac{1}{6}(3a, -\sqrt{3}a, 2c), \\ \mathbf{R}_3 &= \frac{1}{6}(-3a, \sqrt{3}a, 2c).\end{aligned}\quad (1)$$

An example of a shandite crystal structure is shown in Fig. 1(a) with the kagome layers defined by the blue ions. The primitive rhombohedral unit cell is outlined by the light blue arrows while the black arrows denote the conventional hexagonal unit cell. The corresponding Brillouin zones are shown superimposed in Fig. 1(b) and the high-symmetry points F, L, and T that will be relevant in this work, are indicated by arrows. In terms of

BZ point	\mathbf{k} -vector (primitive)	Star of \mathbf{k} (primitive)	\mathbf{k} -vector (conventional)	Little group
F	$(0, \frac{1}{2}, \frac{1}{2})$	$\mathbf{Q}_{F_1} = (0, \frac{1}{2}, \frac{1}{2})$		
		$\mathbf{Q}_{F_2} = (\frac{1}{2}, 0, \frac{1}{2})$	$(-\frac{1}{2}, 0, 1)$	C_{2h} (2/m)
		$\mathbf{Q}_{F_3} = (\frac{1}{2}, \frac{1}{2}, 0)$		
L	$(\frac{1}{2}, 0, 0)$	$\mathbf{Q}_{L_1} = (\frac{1}{2}, 0, 0)$		
		$\mathbf{Q}_{L_2} = (0, \frac{1}{2}, 0)$	$(\frac{1}{2}, \frac{1}{2}, \frac{1}{2})$	C_{2h} (2/m)
		$\mathbf{Q}_{L_3} = (0, 0, \frac{1}{2})$		
T	$(\frac{1}{2}, \frac{1}{2}, \frac{1}{2})$	$\mathbf{Q}_{T_1} = (\frac{1}{2}, \frac{1}{2}, \frac{1}{2})$	$(0, 0, \frac{3}{2})$	D_{3d} (3m)

TABLE I. Relevant high-symmetry points in the Brillouin zone (BZ). The first column shows the high-symmetry point, denoted by the colored arrows in Fig. 1, and the second column shows their coordinate in the primitive basis. The third column denotes the star of each high-symmetry point. The \mathbf{k} -vector of the different points in the conventional unit cell is given in the fourth column, to be compared with the conventional Brillouin zone in Fig. 1. In the last column, we include the little group of each of the high-symmetry points.

the primitive reciprocal lattice vectors,

$$\begin{aligned}\mathbf{G}_1 &= 2\pi(\frac{1}{a}, \frac{\sqrt{3}}{a}, 0), \\ \mathbf{G}_2 &= \pi(\frac{1}{a}, -\frac{\sqrt{3}}{a}, \frac{3}{c}), \\ \mathbf{G}_3 &= \pi(-\frac{3}{a}, -\frac{\sqrt{3}}{a}, \frac{3}{c}).\end{aligned}\quad (2)$$

these points are

$$\begin{aligned}\mathbf{F} &= (0, \frac{1}{2}, \frac{1}{2}), \\ \mathbf{L} &= (0, \frac{1}{2}, 0), \\ \mathbf{T} &= (\frac{1}{2}, \frac{1}{2}, \frac{1}{2}).\end{aligned}\quad (3)$$

Applying the point group operations to these generates the star of each k -point, namely the set of distinct symmetry-equivalent points in the Brillouin zone that are not reachable by a reciprocal lattice vector. These are summarized in Table I. From the table, it is clear that the vectors of the stars obey

$$\begin{aligned}\mathbf{Q}_{F_i} + \mathbf{Q}_{F_j} &= \epsilon_{ijk} \mathbf{Q}_{F_k} \\ \mathbf{Q}_{L_i} + \mathbf{Q}_{L_j} &= \epsilon_{ijk} \mathbf{Q}_{F_k} \\ \mathbf{Q}_{F_i} + \mathbf{Q}_{L_j} &= \epsilon_{ijk} \mathbf{Q}_{L_k},\end{aligned}\quad (4)$$

modulo a reciprocal lattice vector and with ϵ_{ijk} the totally anti-symmetric Levi-Civita symbol.

In the shandites, the kagome layers are formed by transition-metal ions at the $9d$ Wyckoff positions (or $9e$ for a different origin choice) and the states near the Fermi level are dominated by the transition-metal d -electrons (see Sec. IV). We focus on particular shandite materials which exhibit saddle points in the electronic dispersion

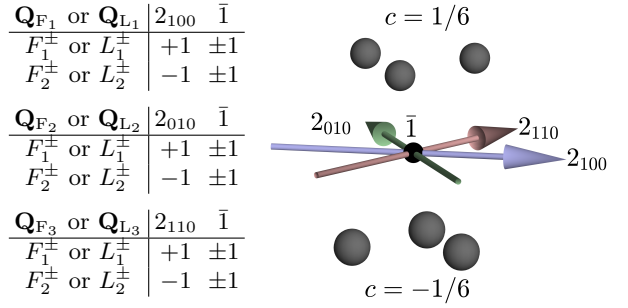


FIG. 2. Characters of the irreps of the little group, C_{2h} , of the F or the L point of $R\bar{3}m$, alongside an illustration of the rotation axes and inversion point with respect to the kagome planes right above the origin at $c = 1/6$ and right below the origin at $c = -1/6$. The table shows the characters of the generators. The little group irreps are one-dimensional, while the corresponding space group irreps are three-dimensional since there are three vectors in the star of F or L. The \pm sign indicates the character under inversion, where the inversion center is placed at the origin of the conventional cell [Fig. 1(a)] in between two kagome layers.

near the F and/or L points shown in Fig. 1(b). These saddle points are accompanied by van Hove peaks in the electronic density of states, although the three-dimensional nature of the shandites prevents the occurrence of true van Hove singularities. Consequently, due to the geometry of the Brillouin zone where the F and L points are connected by vectors in the star of either F or L [Eq. (4)], the regions with large densities of states are nested with each other. Hence, the shandites are promising candidate materials for examining the interplay between structural and electronic degrees of freedom in driving density-wave instabilities with wavevectors at F or L.

III. STRUCTURAL INSTABILITIES IN $R\bar{3}m$ COMPOUNDS

Here, we will focus on the phenomenology of instabilities occurring at the F or L points in the Brillouin zone due to the enhanced nesting between these points. The phenomenology of the transitions that we will consider can be described within Landau theory. The form of the Landau free energy depends solely on the symmetry properties of the order parameters, as given by their space group irreducible representations (irreps). In general, irreps of a symmetry group provide a complete list of different possible order parameters, and the space group irreps of the order parameters contain information on how, in addition to the breaking of the translational symmetry and the related enlargement of the primitive unit cell, the order parameters transform in different ways under the mirrors or rotations of the so-called little group. Consequently, the space group irreps for a specific \mathbf{k}_* -point are constructed from the little group and the star of \mathbf{k}_* . Here, the little group denotes the subgroup of the space group which leaves the wave vector at \mathbf{k}_* invariant

Order	$1\mathbf{Q}(F_1^+)$ (a;0;0)	$3\mathbf{Q}(F_1^+)$ (a;a;a)	$1\mathbf{Q}(L_2^-)$ (b;0;0)	$3\mathbf{Q}(L_2^-)$ (b;b;b)	$1\mathbf{Q}(F_1^+)+2\mathbf{Q}(L_2^-)$ (a;0;0 b;0;b)	$3\mathbf{Q}(F_1^+)+3\mathbf{Q}(L_2^-)$ (a;a;a b;b;b)
Space group	$P2/m$ (#10)	$R\bar{3}m$ (#166)	$C2/m$ (#12)	$R\bar{3}m$ (#166)	$C2/m$ (#12)	$R\bar{3}m$ (#166)
SC size	$1 \times 2 \times 1$	$2 \times 2 \times 1$	$1 \times 2 \times 2$	$2 \times 2 \times 2$	$2 \times 2 \times 2$	$2 \times 2 \times 2$
Ex.						

TABLE II. Space groups resulting from the condensation of different orders that are candidate ground states of the free energy $\mathcal{F}_F + \mathcal{F}_L + \mathcal{F}_{FL}$ relevant for case (i) discussed in the text. The order parameters are shown as phonon displacements that dimerize two of the three kagome atoms. The three consecutive layers in the conventional unit cell are shown, at $c = 1/6$, $c = 1/2$ and $c = 5/6$ along the conventional cell c axis. Notice that the kagome planes are shifted by one of the vectors in Eq. (1) in consecutive layers. In the presence of L order parameters, the unit cell doubles along the conventional c axis, which results in a conventional cell containing six kagome layers. For simplicity, we illustrate only three layers; the remaining three can be envisioned as exhibiting the same phonon modes but with opposite sign.

[69]. The point group of the little group of both the F and L points is C_{2h} ; its generators and their characters are summarized in Fig. 2.

The order parameters are distinguished by whether they are even or odd under the in-plane 2-fold rotations (2_{100} , 2_{010} or 2_{110}) and even or odd under inversion ($\bar{1}$). In addition, order parameters at F or L double the unit cell along specific directions depending on which point in the star the order parameter lies at. For example, the order parameter located at $\mathbf{Q}_{F_1} = (0, \frac{1}{2}, \frac{1}{2})$ would double the rhombohedral unit cell along the b - and c -directions. As a consequence of the little group and the structure of the stars, there are four space group irreps at both the F and L points. These are labeled by F_i^\pm and L_i^\pm , where $i = 1, 2$ labels the number of the irrep and \pm denotes whether it is even or odd under inversion, where the inversion center is placed at the origin of the conventional cell [Fig. 1(a)] in between two kagome layers. As there are three points in the star of both F and L, all the space group irreps are three-dimensional. In contrast, the little group at T is D_{3d} and the space group irreps are labeled by T_i^\pm with $i = 1, \dots, 4$, where the first two are one-dimensional and the last two are two-dimensional. The Landau free energy can be constructed by taking prod-

ucts between the space group irreps and keeping only the terms transforming as the trivial representation Γ_1^+ , i.e. a scalar. This approach is implemented in the INVARIANTS toolkit of the ISOTROPY software suite [70, 71].

We consider two general cases for the coupling between order parameters at F and L. For the first case (i), the order parameter at F transforms as F_1^+ . This has two consequences. It allows the three order parameters at F, deriving from the three points in the star of F, to couple *via* a trilinear term. Moreover, it allows the F and L order parameters to couple through a separate trilinear term, regardless of which irrep the L order parameter transforms as. Consequently, coexistence of F and L orders in this case is favored and their critical temperatures can even be increased. In case (ii), the order parameter at F transforms as F_1^- , F_2^+ , or F_2^- , in which case no trilinear terms are allowed, and the F and L order parameters only couple at quartic order. This implies that coexistence is less robust and generally depends on specific material details.

The analysis of case (i) is more complicated due to the aforementioned trilinear terms. In Table II we depict the atomic displacements of an order parameter transforming as F_1^+ and, for concreteness, an order parameter trans-

forming as L_2^- . This resembles the situation relevant for $\text{Rh}_3\text{Ti}_2\text{S}_2$, discussed in Sec. IV B. Since the space group irreps are three-dimensional, each order parameter will have three components with displacement patterns related to those shown in Table II by symmetry. Denoting the F_1^+ order parameter by $\mathbf{F} = (F_1, F_2, F_3)$ we find

$$\begin{aligned}\mathcal{F}_{F_1^+} &= \frac{\alpha_F}{2}(T - T_F)\mathbf{F}^2 + \frac{\gamma_F}{3}F_1F_2F_3 + \frac{u_F}{4}\mathbf{F}^4 \\ &+ \frac{\lambda_F}{4}(F_1^2F_2^2 + F_1^2F_3^2 + F_2^2F_3^2).\end{aligned}\quad (5)$$

We emphasize that F_i in $\mathbf{F} = (F_1, F_2, F_3)$ do not refer to different irreps, but instead, they refer to the three components of the same irrep F_1^+ . The phase diagram of this free energy has been widely studied in the context of the AV_3Sb_5 kagome metals [42–44]. Importantly, a trilinear term is allowed which promotes simultaneous ordering of all three order parameter components and induces a first-order transition already at the mean-field level. As a consequence, the preferred ground states are those where all three components of \mathbf{F} become non-zero. Borrowing terminology from the transition-metal dichalcogenides and the AV_3Sb_5 kagome metals [10, 20, 42, 72], we refer to these as either trihexagonal or Star-of-David phases, depending on the relative signs of the components of \mathbf{F} . The transition to either of these phases is first-order and the critical temperature is

$$T_{3F} = \frac{2\gamma_F^2}{81\alpha_F(3u_F + \lambda_F)} + T_F.\quad (6)$$

Evidently, for $\gamma_F \neq 0$, $T_{3F} > T_F$, implying that the trihexagonal or Star-of-David configurations are favored over the striped configurations for which only a single order parameter condenses [44]. Note that we take $u_F > 0$ and $3u_F + \lambda_F > 0$ to ensure a bounded free energy. While the striped configurations break the rotational symmetry as described in Table II and doubles the unit cell in two directions, the trihexagonal and Star-of-David configurations do not break any point group symmetries, but only double the unit cell in all $\langle 100 \rangle$ directions. This is similar to the case in the $P6/mmm$ kagome materials.

In similar fashion, denoting an order parameter transforming as L_2^- by $\mathbf{L} = (L_1, L_2, L_3)$, we find the free energy

$$\begin{aligned}\mathcal{F}_L &= \frac{\alpha_L}{2}(T - T_L)\mathbf{L}^2 + \frac{u_L}{4}\mathbf{L}^4 \\ &+ \frac{\lambda_L}{4}(L_1^2L_2^2 + L_1^2L_3^2 + L_2^2L_3^2).\end{aligned}\quad (7)$$

Note that this free energy is the same independent of which irrep \mathbf{L} transforms as. No trilinear term is allowed in this case and, depending on the sign of λ_L , condensation of either a single ($\lambda_L > 0$) or all three components ($\lambda_L < 0$) of \mathbf{L} is favored, resulting in two possible phases.

Their free energies are

$$\mathcal{F}_{1L} = -\frac{\alpha_L^2(T - T_L)^2}{4u_L},\quad (8)$$

$$\mathcal{F}_{3L} = -\frac{\alpha_L^2(T - T_L)^2}{4u_L + \frac{4}{3}\lambda_L},\quad (9)$$

respectively, demonstrating that for $\lambda_L > 0$, the $3L$ phase is favored, while for $\lambda_L < 0$ the $1L$ phase is chosen. Note that, as above, we assume $u_L > 0$ and $3u_L + \lambda_L > 0$ to ensure a bounded free energy. The $1L$ order doubles the unit cell along one $\langle 100 \rangle$ direction, while the $3L$ phase doubles the unit cell in all $\langle 100 \rangle$ directions.

The free energy also allows for trilinear couplings between \mathbf{F} and \mathbf{L} , which favors coexistence of the two orders [42, 44]:

$$\begin{aligned}\mathcal{F}_{F_1^+L} &= \frac{\gamma_{FL}}{3}(F_1L_2L_3 + L_1F_2L_3 + L_1L_2F_3) \\ &+ \frac{\lambda_{FL}^{(1)}}{4}(F_1F_2L_1L_2 + F_1F_3L_1L_3 + F_2F_3L_2L_3) \\ &+ \frac{\lambda_{FL}^{(2)}}{4}(F_1^2L_1^2 + F_2^2L_2^2 + F_3^2L_3^2) + \frac{\lambda_{FL}^{(3)}}{4}\mathbf{F}^2\mathbf{L}^2.\end{aligned}\quad (10)$$

A detailed study of this case is presented in, e.g., Ref. [44]. The main conclusions are that two phases dominate the phase diagram. These are a $3F+3L$ phase, in which all components of \mathbf{F} and \mathbf{L} condense, and a $1F+2L$ phase in which a single component of \mathbf{F} and two components of \mathbf{L} condense. In the former case, the space group remains $R\bar{3}m$ although the unit cell is doubled along all directions, while in the latter case, the order breaks rotational symmetry resulting in the space group $C2/m$ while also doubling the unit cell in all directions. These results are summarized in Table II. The phenomenology of the $R\bar{3}m$ space group exhibits a large variety of possible structural transitions which can occur as a result of a single unstable mode.

In case (ii), where the order parameter at \mathbf{F} transforms as either F_1^- , F_2^+ , or F_2^- , the free energy is simpler as trilinear terms are not allowed. We find

$$\begin{aligned}\mathcal{F}_{F_1^\pm} &= \frac{\alpha_F}{2}(T - T_F)\mathbf{F}^2 + \frac{u_F}{4}\mathbf{F}^4 \\ &+ \frac{\lambda_F}{4}(F_1^2F_2^2 + F_1^2F_3^2 + F_2^2F_3^2),\end{aligned}\quad (11)$$

and

$$\begin{aligned}\mathcal{F}_{F_4^\pm L} &= \frac{\lambda_{FL}^{(1)}}{4}(F_1F_2L_1L_2 + F_1F_3L_1L_3 + F_2F_3L_2L_3) \\ &+ \frac{\lambda_{FL}^{(2)}}{4}(F_1^2L_1^2 + F_2^2L_2^2 + F_3^2L_3^2) + \frac{\lambda_{FL}^{(3)}}{4}\mathbf{F}^2\mathbf{L}^2.\end{aligned}\quad (12)$$

In this case, single components of the \mathbf{F} order parameter can condense even in the absence of fine-tuning. However, since the trilinear terms are absent, whether or not states at \mathbf{F} and \mathbf{L} will coexist depend on specific details and must be decided on a case-by-case basis. This is in contrast to case (i), where the trilinear terms favor coexistence between the orders.

IV. FIRST-PRINCIPLES CALCULATIONS

To assess the role of the electronic degrees of freedom in potential lattice instabilities, we employ first-principles calculations to predict the electronic and crystal structures. Ground state electronic structures are obtained using density-functional theory (DFT) and phonon spectra are evaluated using density-functional perturbation theory (DFPT). Calculations are carried out using Abinit 9.10.1 [73–75], within the Perdew-Burke-Ernzerhof approximation for the solids (PBEsol) [76] and using a basis of projector augmented waves (PAW) with Jollet-Torrent-Holzwarth PAW type pseudo-potentials obtained from PseudoDojo [77–79].

We focus on the family of $M_3A_2\text{Ch}_2$ shandite materials, where M denotes a transition metal while A is a post-transition metal and Ch is a chalcogenide. The transition metal, M , can be Rh, Pd, Ni, or Co. Variants with Co or Ni have been the topic of previous studies [3, 59, 65, 80–82] and we focus on the Rh and Pd realizations. Hence, we calculate the ground state properties for all combinations of $M_3A_2\text{Ch}_2$ with $M = \text{Rh}, \text{Pd}$ and $A = \text{In}, \text{Pb}, \text{Sn}, \text{Tl}, \text{Bi}$ while for the chalcogen we consider either S or Se. In the shandites, the kagome layers are stacked at a $\pi/3$ angle through one of the translations in Eq. (1), resulting in the unit cell shown in Fig. 1(a) and the space group $R\bar{3}m$, as discussed in Sec. II. For each material, we calculate the electronic properties and the lattice response using the fully relaxed primitive rhombohedral unit cell, where the structure is deemed relaxed when the modulus of the forces on the atoms are smaller than 1 meV/Å. We report the relaxed lattice parameters in Tab. III. We use a $16 \times 16 \times 16$ k -point grid and a cutoff energy for the plane-wave basis of 650 eV. Moreover, we converge the ground state Kohn-Sham wavefunctions until the residue squared is less than 10^{-20} eV², such that these can be used to calculate the dynamical matrix at first-order in perturbation theory with DFPT, for which we use a $4 \times 4 \times 4$ q -point grid and a tolerance of 10^{-12} eV in the energy difference as a convergence criterion. For most calculations we use a Gaussian smearing with an electronic smearing temperature of 1 meV, unless stated otherwise.

The electronic structures along the $\Gamma\text{-T}\text{-F}\text{-L}\text{-}\Gamma$ high-symmetry lines with the atomic projections are shown in Fig. 3 for the Ch = S case and in Fig. 4 for the Ch = Se case. These share a number of features: The states near the Fermi level are dominated by the d -orbitals of Rh or Pd, with small contributions from the p -orbitals of the A and Ch ions. We focus on the behavior of the d -orbitals of the M ions forming the kagome layers.

Through the SITESYM tool [83] from the Bilbao Crystallographic Server we check the irreps that are induced by d -orbitals on the Wyckoff positions $9d$ for the space group $R\bar{3}m$. The site symmetry, i.e. the local symmetry of a single atom, is C_{2h} ($2/m$) implying that the d -orbitals split into five singly degenerate states that transform as either the A_g (even under the 2-fold rotation)

Ch	M	A	$a = b = c$ [Å]	$\alpha = \beta = \gamma$ [°]
S	Rh	In	5.549	60.47
		Sn	5.491	61.68
		Tl	5.771	59.67
		Pb	5.677	60.39
	Pd	Bi	5.638	62.61
		In	5.620	61.31
		Sn	5.597	63.10
		Tl	5.846	60.27
Se	Rh	Pb	5.758	62.48
		Bi	5.699	64.47
		In	5.696	59.18
		Sn	5.663	59.76
	Pd	Tl	5.894	58.39
		Pb	5.845	58.71
		Bi	5.811	60.34
		In	5.805	58.72
Se	Pd	Sn	5.805	59.82
		Tl	6.024	58.03
		Pb	5.940	59.71
		Bi	5.891	61.14

TABLE III. Lattice parameters used in the DFT calculations for the rhombohedral unit cell of shandites $M_3A_2\text{Ch}_2$. The parameters were obtained by fully relaxing the unit cell and the atomic positions until the forces on the atoms were smaller than 1 meV/Å in magnitude.

and B_g (odd under the 2-fold rotation) irreps. The particular 2-fold rotation axis is 2_{100} , 2_{010} or 2_{110} depending on which of the three kagome atoms is considered. The induced irreps at the F, L, Γ , and T points, as well as the Λ line (Λ denotes the line connecting Γ and T), are shown in Table IV. Examples of the corresponding (real) wavefunctions are shown in Fig. 5 for the points Γ and F on a single layer. The T and L irreps can be readily obtained by replicating the wavefunctions with a π phase-shift on consecutive layers.

The bands of $M_3A_2\text{Ch}_2$ on the $\Gamma\text{-T}\text{-F}\text{-L}\text{-}\Gamma$ line generally come in two varieties. The first is bands that are two-fold degenerate on the $\Gamma\text{-T}$ (Λ) line and derive from the Γ_3^+ irrep at Γ , the T_3^- irrep at T, and the Λ_3 irrep at a general point on the line. At the F point this splits into one of the one-dimensional F irreps (here we are talking about the irreps of a *single* F point of the star, hence these are one-dimensional). The second variety is bands that are one-dimensional, non-degenerate by symmetry through the whole line and thus only exhibit accidental degeneracies (if any). The least dispersive bands on the Λ line, some of which are completely flat, derive from the A_g orbitals simultaneously present on all three kagome atoms, transforming like Γ_1^+, Λ_1 and T_2^- . Such flat bands appear very close to the Fermi level in some of the Rh compounds, but well below it in the Pd compounds, as can be seen by contrasting the first and second column in Figs. 3 and 4. The more dispersive bands on the Λ line come from B_g orbitals forming either one-dimensional Γ_2^+, Λ_2 , and T_1^- states or the two-dimensional Γ_3^+, Λ_3 , and T_3^- states.

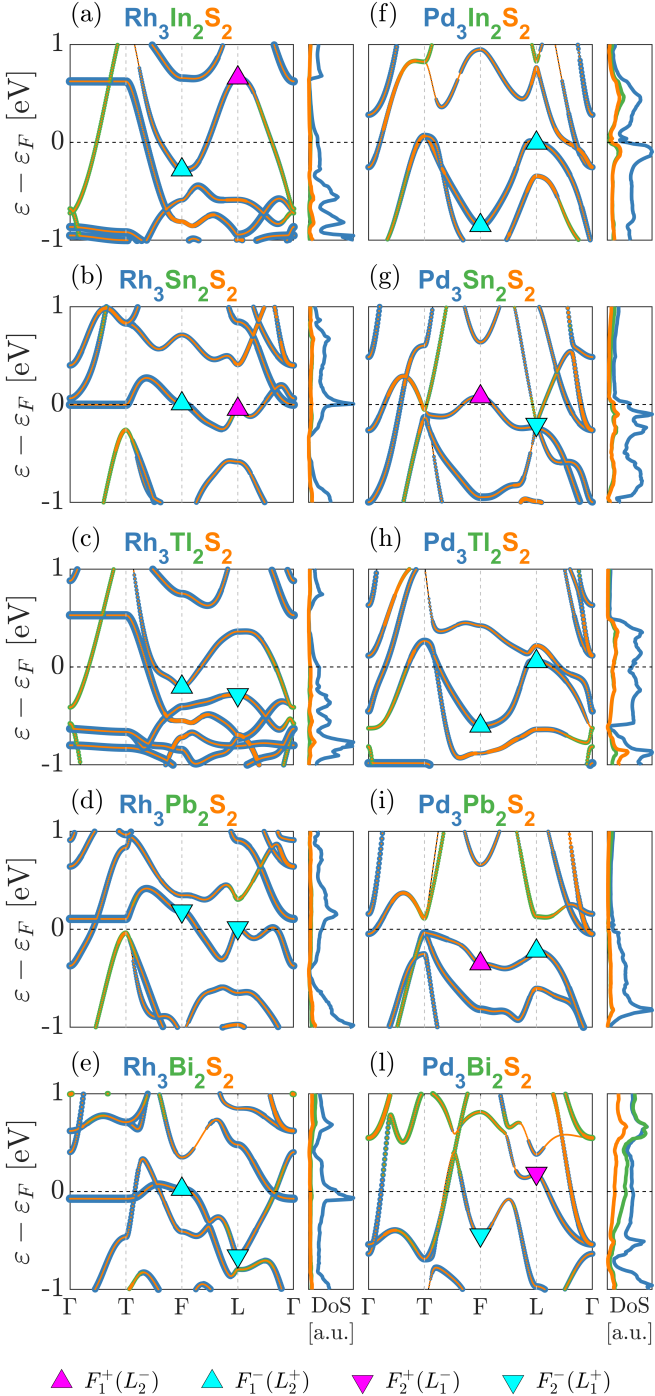


FIG. 3. Orbitally resolved electronic structures of shandite materials $M_3A_2S_2$ for (a)–(e) $M=\text{Rh}$ and (f)–(l) $M=\text{Pd}$. Different colors correspond to different orbital weights. Blue denotes the d -orbitals of the M atoms, green the p -orbitals of the A atoms while orange shows the p -orbitals of the S atoms. The irreducible representations $F_{1,2}^\pm$ and $L_{1,2}^\pm$ of the states closer to the Fermi level are shown with magenta (+) or cyan (-) triangles pointing upwards (1) or downwards (2). The orbitally resolved electronic density of states is attached to the right of each figure.

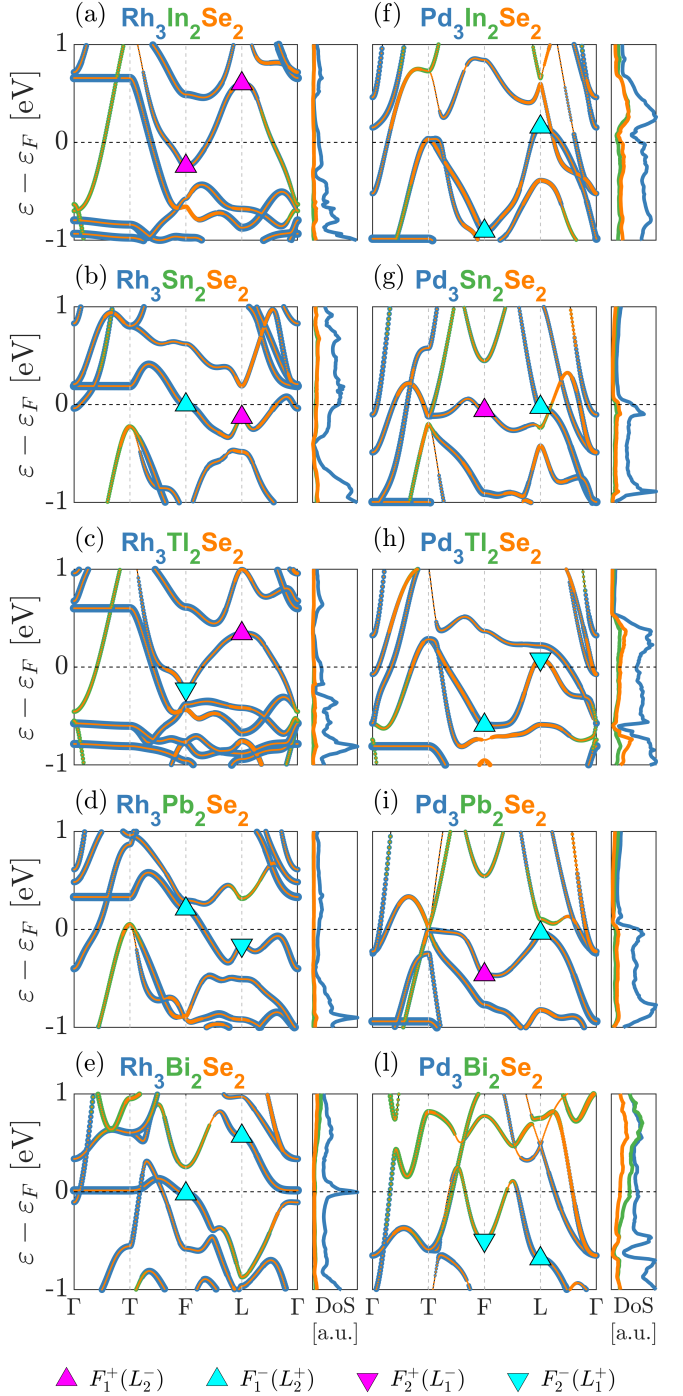


FIG. 4. Orbitally resolved electronic structures of shandite materials $M_3A_2Se_2$ for (a)–(e) $M=\text{Rh}$ and (f)–(l) $M=\text{Pd}$. Different colors correspond to different orbital weights. Blue denotes the d -orbitals of the M atoms, green the p -orbitals of the A atoms while orange shows the p -orbitals of the Se atoms. The irreducible representations $F_{1,2}^\pm$ and $L_{1,2}^\pm$ of the states closer to the Fermi level are shown with magenta (+) or cyan (-) triangles pointing upwards (1) or downwards (2). The orbitally resolved electronic density of states is attached to the right of each figure.

P_Γ (D_{3d})	Subduced irrep	M d-orbitals
Γ_1^+	A_g	$d_{xy} + d_{x^2-y^2} + d_{z^2}$
Γ_2^+	B_g	$d_{xz} + d_{yz}$
Γ_3^+	$A_g \oplus B_g$	$d_{xy} + d_{x^2-y^2} + d_{z^2} + d_{xz} + d_{yz}$
P_F (C_{2h})	Subduced irrep	M d-orbitals
F_1^+	A_g	$d_{xy} + d_{x^2-y^2} + d_{z^2}$
F_2^+	B_g	$d_{xz} + d_{yz}$
F_1^-	$A_g \oplus B_g$	$d_{xy} + d_{x^2-y^2} + d_{z^2} + d_{xz} + d_{yz}$
F_2^-	$A_g \oplus B_g$	$d_{xy} + d_{x^2-y^2} + d_{z^2} + d_{xz} + d_{yz}$
P_L (C_{2h})	Subduced irrep	M d-orbitals
L_1^+	$A_g \oplus B_g$	$d_{xy} + d_{x^2-y^2} + d_{z^2} + d_{xz} + d_{yz}$
L_2^+	$A_g \oplus B_g$	$d_{xy} + d_{x^2-y^2} + d_{z^2} + d_{xz} + d_{yz}$
L_1^-	B_g	$d_{xz} + d_{yz}$
L_2^-	A_g	$d_{xy} + d_{x^2-y^2} + d_{z^2}$
P_T (D_{3d})	Subduced irrep	M d-orbitals
T_1^-	B_g	$d_{xz} + d_{yz}$
T_2^-	A_g	$d_{xy} + d_{x^2-y^2} + d_{z^2}$
T_3^-	$A_g \oplus B_g$	$d_{xy} + d_{x^2-y^2} + d_{z^2} + d_{xz} + d_{yz}$
P_Λ (C_{3v})	Subduced irrep	M d-orbitals
Λ_1	A_g	$d_{xy} + d_{x^2-y^2} + d_{z^2}$
Λ_2	B_g	$d_{xz} + d_{yz}$
Λ_3	$A_g \oplus B_g$	$d_{xy} + d_{x^2-y^2} + d_{z^2} + d_{xz} + d_{yz}$

TABLE IV. Space group irreps at the F, L, Γ , T and Λ points of $R\bar{3}m$ and the corresponding subduced representation at C_{2h} ($2/m$), the site symmetry of the Wyckoff position 9d. For Γ only the inversion-even irreps are shown since the space group is centrosymmetric. The Λ points are on the Γ -T line.

At the F and L points, there are only four possible states $F_{1,2}^\pm$ and $L_{1,2}^\pm$. When combining the transformation properties under the point group irreps with the translational ones imposed by the F and L points, one can infer how the Bloch states localize on specific kagome atoms within a single unit cell. As shown in Fig. 5, the $F_1^-(L_2^+)$ and $F_2^-(L_1^+)$ states arise from contributions across all orbitals and are distributed over two of the three atoms, a result of the ‘mixed’ nature of the van Hove points. In contrast, $F_1^+(L_2^-)$ consists solely of A_g orbitals localized on a single atom, while $F_2^+(L_1^-)$ is composed exclusively of B_g orbitals, also confined to a single atom. These are examples of ‘pure’ type van Hove points.

The phonon spectra of $M_3A_2\text{Ch}_2$ shandites exhibit distinct energy-dependent contributions from the constituent atoms. At low energies, the spectra are domi-

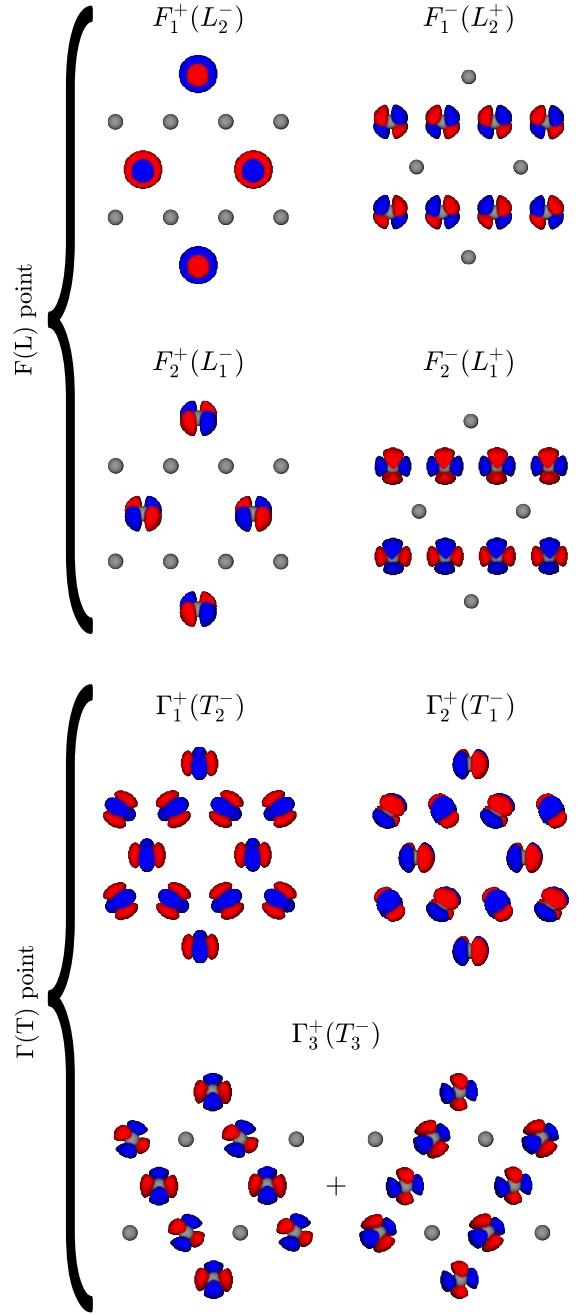


FIG. 5. Some examples of the wavefunctions induced by the d-orbitals of the atoms forming the kagome layers in shandites at the high-symmetry points Γ , T, F and L, and their irreps. While these wavefunctions, shown on a single layer of the conventional cell at $c = 1/2$, are obtained from DFT, their forms are consistent with group theory predictions. The corresponding Wyckoff position, 9d, has local symmetry C_{2h} ($2/m$) so that the d-orbitals split into the A_g (even under 2_{100}) and B_g (odd under 2_{100}) irreps. Note that the periodicity of these wavefunctions between different layers are different according to their different wavevectors.

nated by phonon modes primarily involving the motion of the heavier M and A ions, while at higher energies, the

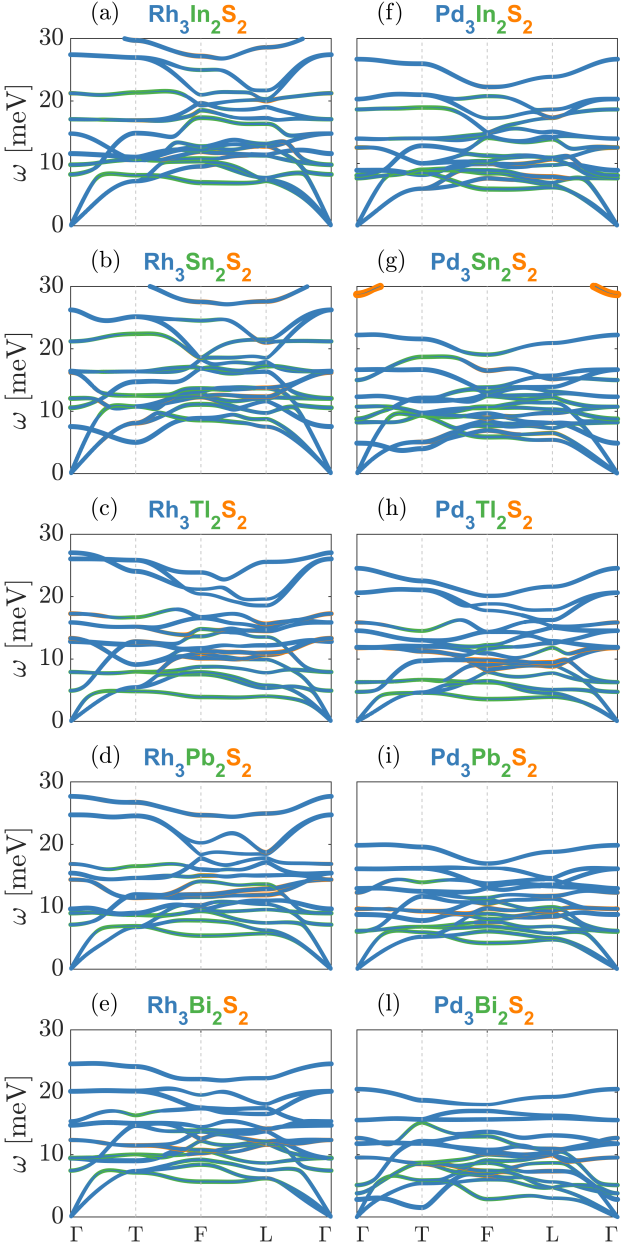


FIG. 6. Phonon spectra of shandite materials $M_3A_2S_2$, with contributions from different atomic species highlighted: blue represents displacement primarily from M atoms, green corresponds to A atoms, and orange denotes S atoms. Higher energy phonons, completely dominated by the motion of the S ions, are not shown.

vibrations of the Ch ions become predominant, owing to their lighter masses. This behavior is illustrated in Fig. 6 and Fig. 7. A general trend is observed wherein certain phonon modes associated with the M ions display dips at the T point. Nevertheless, for most of the studied compounds, the phonon spectra remain stable indicating that no structural instabilities nor charge orders are predicted by DFT at ambient conditions. The sole exception is $\text{Rh}_3\text{Sn}_2\text{Se}_2$, which exhibits an unstable T_2^+ phonon

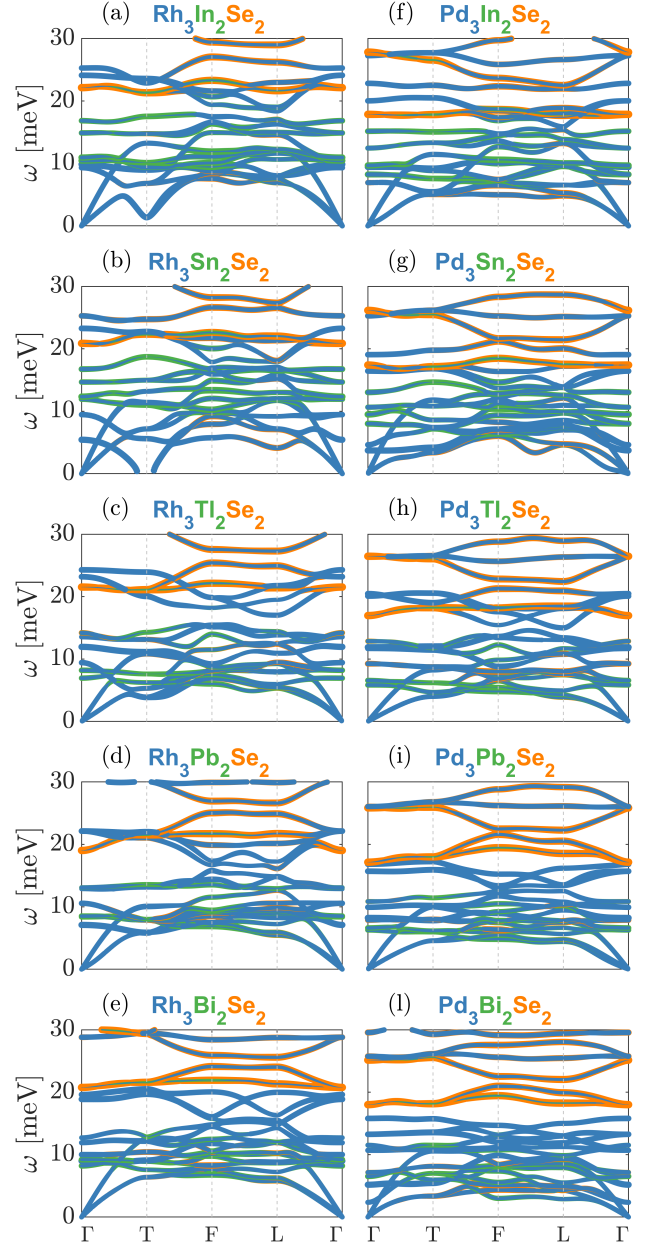


FIG. 7. Phonon spectra of shandite materials $M_3A_2\text{Se}_2$, with contributions from different atomic species highlighted: blue represents displacement primarily from M atoms, green corresponds to A atoms, and orange denotes Se atoms. Higher energy phonons, completely dominated by the motion of the Se ions, are not shown.

mode. We attribute this exception to a purely structural instability, as will be explained later. To probe how these predictions relate to the electronic degrees of freedom, we focus on materials featuring F or L states near the Fermi level and away from the Γ - T flat bands. These criteria are met by the materials $\text{Rh}_3\text{Tl}_2\text{S}_2$, $\text{Pd}_3\text{Sn}_2\text{S}_2$, and $\text{Pd}_3\text{Pb}_2\text{S}_2$, as shown in Figs. 3(c), (g), and (i), respectively, as well as $\text{Rh}_3\text{Sn}_2\text{Se}_2$ and $\text{Pd}_3\text{Sn}_2\text{Se}_2$, as depicted in Figs. 4(b) and (g).

Using simulated doping and simulated hydrostatic pressure, the energy of the F and L states can be tuned across the Fermi level thus allowing for the study of the potential correlation between the position of the electronic states and the appearance of any unstable phonon modes. Doping is simulated by introducing a background charge corresponding to a fraction of an electron, uniformly distributed in the unit cell, such that the charge density is $n_x(\mathbf{r}) = n(\mathbf{r}) + ex$, where $-e$ is the elementary charge of the electron and x represents the fraction of added charge. Consequently, positive x corresponds to hole doping and vice versa. We note that this approach of simulated doping is only justifiable if x is kept small. After introducing the background charge, we do not perform any further structural relaxation. Pressure is simulated by imposing that the diagonal elements of the stress tensor reach a target value of $-P$, corresponding to the magnitude of the hydrostatic pressure, when relaxing the crystal structure of the material being studied.

A. Structurally stable compounds: $\text{Pd}_3\text{Sn}_2\text{S}_2$, $\text{Pd}_3\text{Pb}_2\text{S}_2$, and $\text{Rh}_3\text{Sn}_2\text{Se}_2$

It is instructive to first consider the cases where doping or pressure fails to induce a structural distortion. Fig. 8 shows the effects of doping and pressure on $\text{Pd}_3\text{Sn}_2\text{S}_2$, $\text{Pd}_3\text{Pb}_2\text{S}_2$, and $\text{Rh}_3\text{Sn}_2\text{Se}_2$. In addition to the changes in the electronic structure, we calculate the doping-dependence of the lowest frequency phonon mode at the F and L points respectively, as well as the Lindhard function. The Lindhard function is a measure of the nesting of the electronic structure, and it is given by

$$\mathcal{L}(q) = \frac{1}{N_b^2 N_k} \Re \left\{ \sum_{nm\mathbf{k}} \frac{n_F(\varepsilon_{n\mathbf{k}+\mathbf{q}}) - n_F(\varepsilon_{m\mathbf{k}})}{\varepsilon_{m\mathbf{k}} - \varepsilon_{n\mathbf{k}+\mathbf{q}} + i\eta} \right\}, \quad (13)$$

where $\varepsilon_{n\mathbf{k}}$ is the energy of band n at momentum \mathbf{k} and $n_F(\cdot)$ denotes the Fermi-Dirac distribution function where we use an electronic temperature of 1 meV. The expression is normalized by the number of bands N_b^2 and the number of k -points sampled N_k . We selected all the bands in a window of 2 eV around the Fermi level. For the artificial smearing we use $\eta \approx 10^{-3}$ meV, corresponding to the average separation of the energy eigenstates. To calculate the Lindhard function, we evaluated the eigenvalues on a finer $32 \times 32 \times 32$ k -point grid through a one-shot non-selfconsistent DFT calculation, so that $N_k = 32^3$. In the one-band case, Eq. (13) is precisely the non-interacting susceptibility. In multi-orbital systems, matrix elements quantifying the degree of overlap between the states connected by \mathbf{q} also play a role. However, these are omitted here, as we focus solely on whether the electronic structure exhibits increased or decreased nesting as the electronic content is varied.

Doping moves the electronic states at F and/or L closer to the Fermi level and leads to a crossing for a specific value of x , particular to the material [see Figs. 8(a), (d),

and (j)]. In the case of $\text{Pd}_3\text{Sn}_2\text{S}_2$, electron doping shifts the F_1^+ state closer to the Fermi level. As shown in Figs. 8(c), the Lindhard function exhibits a relative peak at the L point that seems to be suppressed as the band is moved below the Fermi level. As seen in Fig. 8(b), no concomitant softening of the phonon modes is observed and the material remains stable within this doping range.

For $\text{Pd}_3\text{Pb}_2\text{S}_2$ electron doping shifts both the F_1^+ and L_2^+ states closer to the Fermi level, as shown in Fig. 8(d). While the Lindhard function, shown in Fig. 8(f) is enhanced slightly for large values of electron doping, with a few peaks forming, this is for values of x corresponding to adding more than one electron per unit cell. This is beyond the range where the simple method we used to simulate doping is deemed justifiable and does not result in any of the phonon modes becoming unstable, as seen in Fig. 8(e).

In $\text{Rh}_3\text{Sn}_2\text{Se}_2$, the F_1^+ state appears at the Fermi level and any doping shifts it further away. In contrast, the L_2^- state is shifted closer to the Fermi level by hole doping, as shown in Fig. 8(j). Thus, hole doping leads to the formation of a peak near L in the Lindhard function [Fig. 8(l)], although the F and L point phonons remain stable throughout the doping range, as shown in Fig. 8(k). This peak is observed for the substantially hole doped case, which is beyond the validity of the background charge method. While $\text{Rh}_3\text{Sn}_2\text{Se}_2$ does exhibit an unstable T_2^+ phonon mode at T. However, as shown in Fig. 9, this is unaffected by the electronic smearing temperature, and we therefore attribute this to a structurally driven transition. As seen in Fig. 8(k), a relatively small amount of electron doping also renders the T_2^+ phonon mode stable.

Applying hydrostatic pressure shifts the electronic states of $\text{Pd}_3\text{Pb}_2\text{S}_2$ and $\text{Rh}_3\text{Sn}_2\text{Se}_2$ closer to the Fermi level. In contrast, hydrostatic pressure on $\text{Pd}_3\text{Sn}_2\text{S}_2$ has the effect of moving the F_1^+ state away from the Fermi level, so we do not consider it here. In the case of $\text{Pd}_3\text{Pb}_2\text{S}_2$, a large pressure of $P \approx 42$ GPa is required to shift the F_1^+ state to the Fermi level [see Fig. 8(g)]. The Lindhard function [Figs. 8(i) and (o)] is generally suppressed and develops no new features under pressure. Moreover, the L and F point phonons remain stable under pressure [as shown in Figs. 8(h) and (n)], and the T_2^+ mode of $\text{Rh}_3\text{Sn}_2\text{Se}_2$ becomes stable near $P \approx 4$ GPa, as shown in Fig. 8(n).

B. Instabilities in $\text{Rh}_3\text{Tl}_2\text{S}_2$ and $\text{Pd}_3\text{Sn}_2\text{Se}_2$

Details of the first-principles results on $\text{Rh}_3\text{Tl}_2\text{S}_2$ are presented in Fig. 10. The electronic structure is dominated by the Rh d -orbitals as shown in Fig. 3(c), although the S p -orbitals are prevalent in the states near the L point. Neither the F_1^+ or L_1^+ states nearest to the Fermi level are accompanied by a peak in the density of states. Nevertheless, hole doping [Figs. 10(a) and (b)] induces a structural instability near $x = 1$, when F_1^+ lies

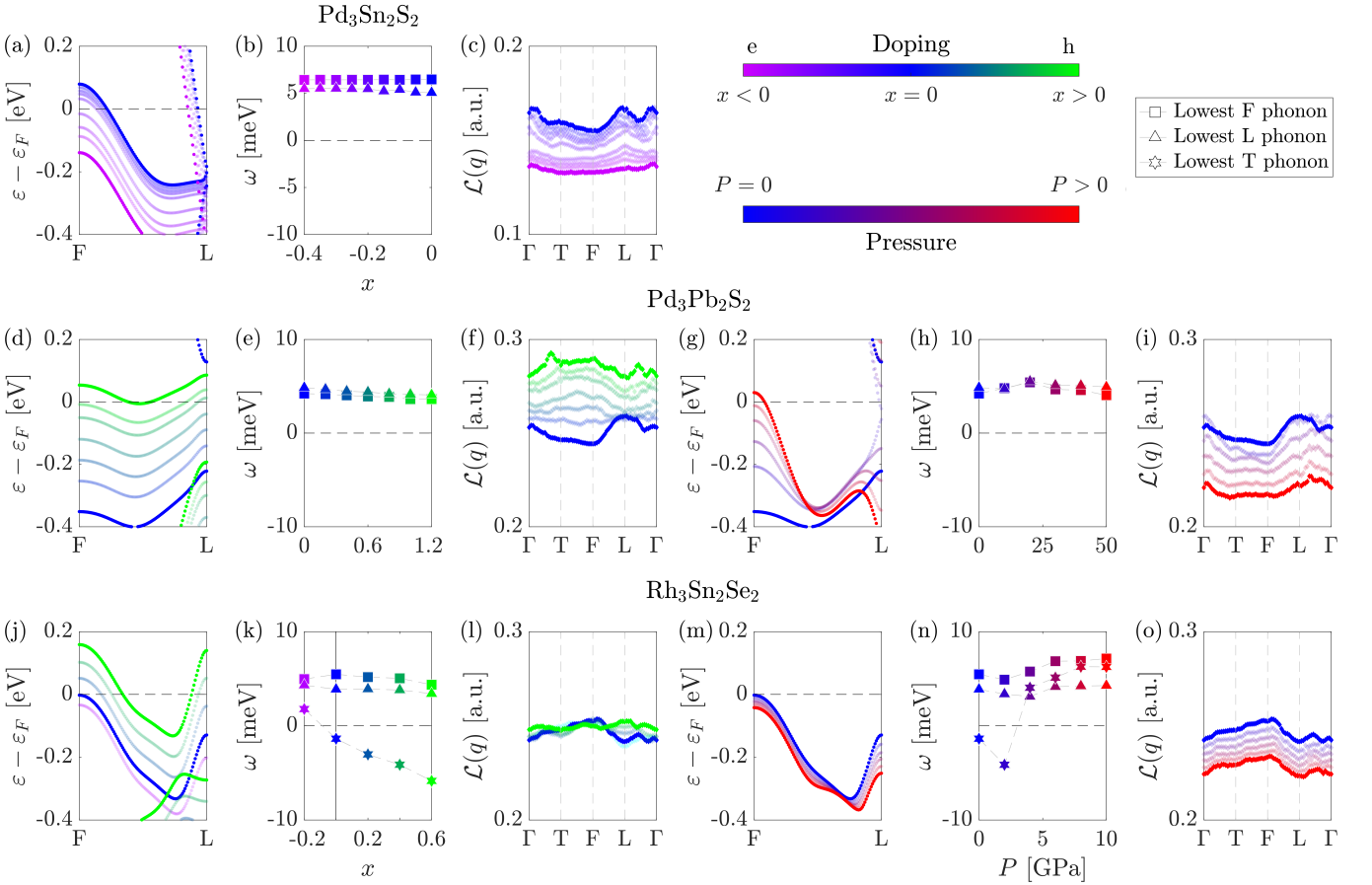


FIG. 8. Band structure, phonon frequencies and Lindhard function of (a)–(c) $\text{Pd}_3\text{Sn}_2\text{S}_2$, (d)–(i) $\text{Pd}_3\text{Pb}_2\text{S}_2$ and (j)–(o) $\text{Rh}_3\text{Sn}_2\text{Se}_2$ under doping and pressure. Imaginary frequencies are represented as negative numbers for easier visualization. For $\text{Rh}_3\text{Sn}_2\text{Se}_2$, the T point phonon mode is stabilized by electron doping (k), or by pressures exceeding 4 GPa (n).

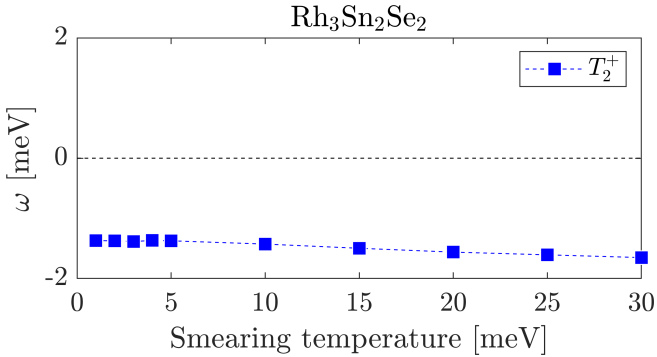


FIG. 9. Dependence on the electronic smearing temperature of the unstable T_2^+ phonon mode of $\text{Rh}_3\text{Sn}_2\text{Se}_2$. The nearly flat behavior indicates that the transition is driven primarily by structural degrees of freedom rather than electronic. Here, imaginary frequencies are represented by real negative numbers for easier visualization.

at the Fermi level. Once again, this is taking the doping method beyond its realm of reliability when comparing to experiments, but the fact that a change in the Fermi

level leads to soft phonon mode hints at the interplay between structural and electronic degrees of freedom in this compound, especially when combined with the fact that the instability disappears when increasing the electronic smearing temperature, as shown in Fig. 11. In spite of this, the Lindhard function, shown in Fig. 10(c) is featureless and exhibits no enhancement as the structural instability is approached. We note that the smearing temperature for which the phonon becomes stable, ~ 3 meV in Fig. 11, should not be interpreted as the transition temperature of the structural transition. As shown in Ref. [48], anharmonic contributions will generally impact the transition temperature. Rather, the strong dependence of the phonon frequency on the electronic smearing demonstrates that the electrons play an important role in driving the structural deformation.

The soft phonon mode is a L_2^- mode associated with the distortion pattern illustrated in Fig. 10(d). When this mode is stable, it primarily involves out-of-plane motion of the Rh ions. However, as the phonon frequency becomes imaginary, the mode evolves into a pattern resembling that shown in Tab. II, characterized predominantly by in-plane motion of the Rh ions in a dimerized

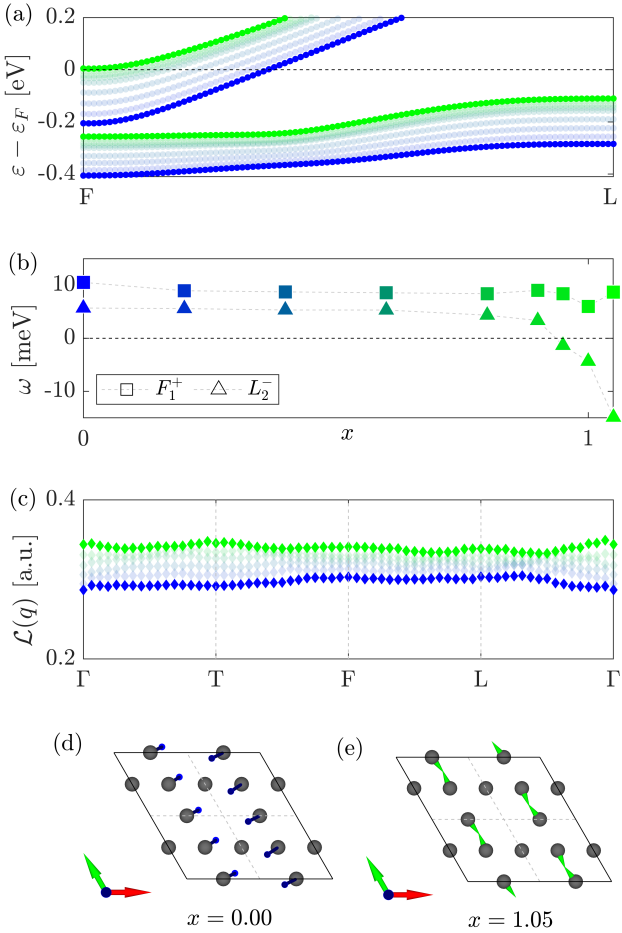


FIG. 10. $\text{Rh}_3\text{Tl}_2\text{S}_2$ under simulated hole doping. (a) Electronic band structure between the F and L points as a function of doping. (b) Lowest energy phonon modes at the F and L points as a function of doping. Negative values represent imaginary frequencies. (c) Bare electronic susceptibility in the constant matrix element approximation, as a function of doping. (d) Lowest energy L_2^- phonon mode at $x = 0$ (stable) and at $x = 1$ (unstable).

configuration. As explained in Sec. III, the free energy is minimized by a state where either a single mode or three modes condense simultaneously. In the former case, the symmetry is lowered to $C2/m$, while in the latter the space group remains $R\bar{3}m$, although the unit cell is doubled along all three lattice directions.

Here, the lowest phonon mode at F is an F_1^+ mode. Hence, this corresponds to case (i) for the free energy studied in Sec. III. Consequently, it is possible that the condensation of the L_2^- order results in a secondary transition of an F_1^+ order. Determining whether or not this is the case would require calculating the energy of the appropriately distorted lattice as done, e.g., in Ref. [46, 49] for the kagome metals.

Like $\text{Rh}_3\text{Tl}_2\text{S}_2$, the electronic structure of $\text{Pd}_3\text{Sn}_2\text{Se}_2$ near the Fermi level is dominated by electronic d -orbitals, in this case originating from Pd, as shown in Fig. 4(g).

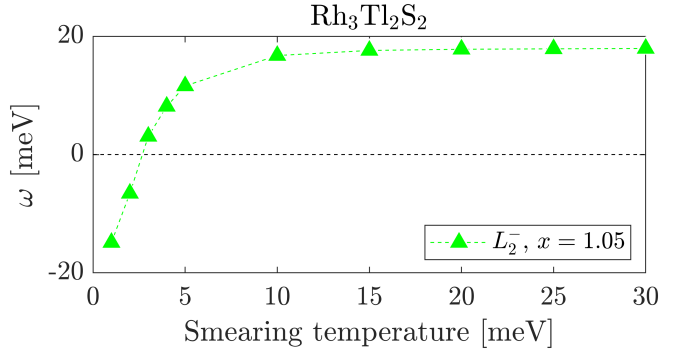


FIG. 11. Dependence of the unstable phonon modes frequency on the electronic smearing temperature for the L_2^- phonon mode in electron doped $\text{Rh}_3\text{Tl}_2\text{S}_2$ at $x = 1.05$. The sharp dependence on electronic temperature suggests a transition driven primarily by the electronic degrees of freedom. Imaginary frequencies are represented as negative numbers for easier visualization.

The density of states exhibits a prominent peak immediately below the Fermi level, and the electronic structure features segments of near-flat bands between F and L and between L and T. As shown in Figs. 12(c) and (d), both hole doping and hydrostatic pressure induce structural transitions in this material.

In the case of hole doping, a soft acoustic mode with symmetry L_1^+ appears near $x \approx 0.15$ and $x \approx 0.25$, with an intermediate stable region. These instabilities occur at around the same doping level where the electronic states F_1^+ and L_2^+ , respectively, cross the Fermi level. As in the previous cases, the Lindhard function remains nearly featureless and exhibits no enhancements near these doping levels. Hydrostatic pressure also leads to soft modes, with both an L_1^+ and an F_2^+ mode becoming soft near 2 GPa and 4 GPa, respectively. As with doping, these instabilities are concomitant with states at F and L crossing the Fermi level while the Lindhard function remains featureless. Differently from the case of $\text{Rh}_3\text{Tl}_2\text{S}_2$, the two unstable phonon modes do not experience significant changes after becoming unstable, and they distort the kagome lattice as shown in Figs. 12(g) and (h).

To further probe the interplay between the structural and electronic degrees of freedom, we performed the above calculations at different electronic smearing temperatures. The results are shown in Fig. 13. As the electronic smearing temperature is increased, the instability under hole doping disappears, thus indicating that the electrons themselves play a role in driving the structural instability [Fig. 13(a)], despite the fact that the Lindhard function exhibits no peaks near the relevant high symmetry points. The instability under pressure shows a noticeable dependence on the smearing temperature only at low temperatures [Fig. 13(b)]. This behavior contrasts with that of $\text{Rh}_3\text{Sn}_2\text{Se}_2$, shown in Fig. 9, and suggests that hydrostatic pressure may partially stabilize the structural instability compared to the hole-doped case, possibly sug-

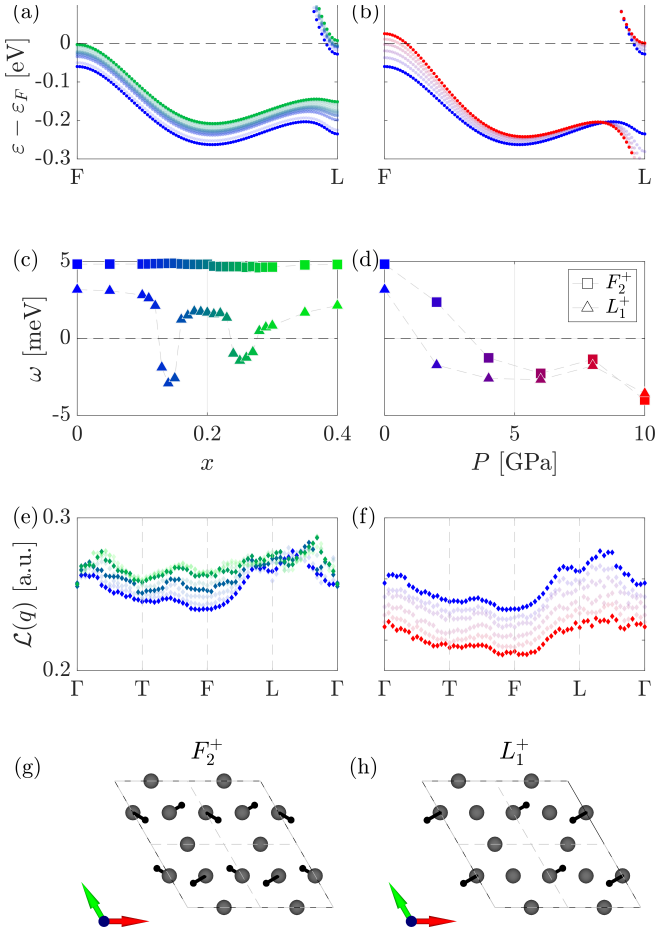


FIG. 12. Pd₃Sn₂Se₂ under simulated hole doping and hydrostatic pressure. (a–b) Electronic band structure in the line between the F and L point as a function of hole doping and hydrostatic pressure. (c–d) Lowest energy phonon modes at the F and L points as a function of hole doping and hydrostatic pressure. Negative values represent imaginary frequencies. (e–f) Bare electronic susceptibility in the constant matrix element approximation, as a function of hole doping and hydrostatic pressure. (g–h) Lowest energy phonon modes that become unstable under doping or pressure at the F point (g) and at the L point (h).

gesting that a different mechanism is at play.

The L₁⁺ phonon mode is illustrated in Fig. 12(h) and the main distinction from an F-point phonon mode is the additional out-of-phase modulations between neighboring kagome layers. As discussed in Sec. III, instabilities at the L point can lead to two distinct phases, depending on whether one or three L modes condense. In the case of the condensation of a single L₁⁺ mode, the three-fold improper rotation symmetry is broken, and the space group is reduced to C2/m (#12). If three L₁⁺ modes condense, the unit cell doubles in all lattice directions while the space group remains R̄3m. An F-point mode can condense in addition to the L modes. This can happen in two distinct ways: either through a secondary transition as in Fig. 12(d) resulting from a soft phonon mode or

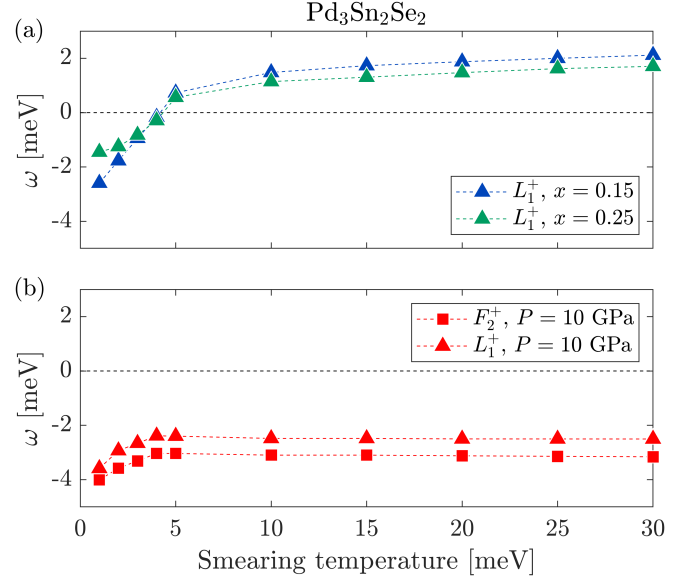


FIG. 13. Dependence of the unstable phonon modes frequency on the electronic smearing temperature for (a) the L₁⁺ phonon mode in electron doped Pd₃Sn₂Se₂ at x = 0.15 and x = 0.25, indicating a transition driven primarily by electronic degrees of freedom (b) the L₁⁺, F₂⁺ phonon modes in Pd₃Sn₂Se₂ under 10GPa of hydrostatic pressure. The flat behavior suggests that the transition is driven by the structural degrees of freedom, in contrast to the hole doped scenario. Imaginary frequencies are represented as negative numbers for easier visualization.

by being induced by the L order through the couplings discussed in Sec. III. Here, the lowest phonon mode at the F point transforms as F₂⁺, implying that there is no trilinear coupling to the condensed L₁⁺ mode, corresponding to case (ii) discussed in Sec. III. In this case, whether coexistence of the two orders is favored depends on the specific parameters of the free energy. To determine if an additional order condenses as a result of the L₁⁺ mode, one should compute the energy of the different crystal structures which is beyond the scope of the current manuscript.

V. CONCLUSIONS AND DISCUSSION

In this work, we carried out a detailed study of possible electronically driven structural phase transitions in Pd- and Rh-based kagome-layered shandites. Combining DFT and DFPT we calculated the electronic structure and the phonon spectra for 20 shandite candidate materials crystallizing in the R̄3m space group. The electronic structures are dominated by the Pd or Rh d-electrons and feature van Hove points at the F and L points in the Brillouin zone, and in many of the Rh-based compounds a flat band appears near the Fermi level between the Γ and T points. All combinations studied save one were found to be stable, i.e., only one exhibited an imaginary fre-

frequency phonon. The unstable material, $\text{Rh}_3\text{Sn}_2\text{Se}_2$, features an unstable T_2^+ phonon mode and while this leads to an increase in the unit cell, it does not alter the space group.

Motivated by the possible interplay between van Hove points and electronically driven structural transitions, we selected five of the compounds which featured van Hove points at F or L near the Fermi level while simultaneously having the flat Γ -T band further from the Fermi level. Doping or hydrostatic pressure can shift the van Hove points of these compounds to the Fermi level and in two of the cases, the materials become unstable with an imaginary L point phonon mode. $\text{Rh}_3\text{Ti}_2\text{S}_2$ becomes unstable under significant hole doping, corresponding to the amount needed to shift the electronic states at F to the Fermi level [see Figs. 10(a) and (b)]. However, this requires going beyond the region where our method of adding a background charge to the system to simulate doping is valid. In contrast, $\text{Pd}_3\text{Sn}_2\text{Se}_2$ becomes unstable for smaller values of hole doping, consistent with the regions where either the electronic states at L or at F reaches the Fermi level which, in both cases, result in an unstable L point phonon mode, as shown in Fig. 12(c). Furthermore, the electronic states are also shifted towards the Fermi level by hydrostatic pressure, which also leads to unstable phonon modes in the system, as shown in Fig. 12(d). To further highlight the role played by the electrons in driving these phonons unstable, we considered the impact of the electronic smearing temperature on the phonon frequencies. In the cases where the structural transitions are concomitant with van Hove points appearing at the Fermi level, i.e., for hole-doped $\text{Rh}_3\text{Ti}_2\text{S}_2$ and $\text{Pd}_3\text{Sn}_2\text{Se}_2$, increasing the electronic smearing hardens the unstable phonon mode until it becomes stable at sufficiently large values of the smearing, as shown in Fig. 11 and 13(a). This is in contrast to the behavior observed in $\text{Rh}_3\text{Sn}_2\text{Se}_2$ and $\text{Pd}_3\text{Sn}_2\text{Se}_2$ un-

der pressure where the frequency of the unstable phonon is nearly unaffected by the electronic smearing [Fig.9 and Fig.13(b)].

We interpret the above results to indicate that electronic correlations can drive structural instabilities in specific shandites, specifically in $\text{Rh}_3\text{Ti}_2\text{S}_2$ and $\text{Pd}_3\text{Sn}_2\text{Se}_2$. However, moving the van Hove points at the F or L points to the Fermi level in other shandites, including $\text{Pd}_3\text{Sn}_2\text{S}_2$, $\text{Pd}_3\text{Pb}_2\text{S}_2$, and $\text{Rh}_3\text{Sn}_2\text{Se}_2$, does not result in a structural transition, implying that additional effects may play a role. To capture these, it may be necessary to include the effect of the motion of the apical chalcogen ions or the impact of electronic interactions on the electronic and phononic spectra through, e.g., DFT+ U calculations. Nevertheless, the fact that the structural transitions in $\text{Rh}_3\text{Ti}_2\text{S}_2$ and $\text{Pd}_3\text{Sn}_2\text{Se}_2$ vanish when the electronic smearing is increased is evidence that the electronic degrees of freedom are driving the transition. This is further supported by the fact that the transitions occur once the van Hove points are moved to the Fermi level. We hope these theoretical results will engender future experiments on the shandite compounds. As we have shown here, these materials host a promising interplay between lattice vibrations and correlated electrons driven by the unique kagome structure.

ACKNOWLEDGMENTS

M.H.C. is supported by ERC grant project 101164202 – SuperSOC. Funded by the European Union. Views and opinions expressed are however those of the authors only and do not necessarily reflect those of the European Union or the European Research Council Executive Agency. Neither the European Union nor the granting authority can be held responsible for them. Work at the University of Minnesota (L.B. and T.B.) were supported by the NSF CAREER grant DMR-2046020.

-
- [1] J.-X. Yin, B. Lian, and M. Z. Hasan, Topological kagome magnets and superconductors, *Nature* **612**, 647 (2022).
- [2] T. Neupert, M. M. Denner, J.-X. Yin, R. Thomale, and M. Z. Hasan, Charge order and superconductivity in kagome materials, *Nature Physics* **18**, 137 (2022).
- [3] E. Liu, Y. Sun, N. Kumar, L. Muechler, A. Sun, L. Jiao, S.-Y. Yang, D. Liu, A. Liang, Q. Xu, J. Kroder, V. Süß, H. Borrmann, C. Shekhar, Z. Wang, *et al.*, Giant anomalous Hall effect in a ferromagnetic kagome-lattice semimetal, *Nature Physics* **14**, 1125 (2018).
- [4] B. R. Ortiz, S. M. L. Teicher, Y. Hu, J. L. Zuo, P. M. Sarte, E. C. Schueller, A. M. M. Abeykoon, M. J. Krogstad, S. Rosenkranz, R. Osborn, R. Seshadri, L. Balents, J. He, and S. D. Wilson, CsV_3Sb_5 : A \mathbb{Z}_2 Topological Kagome Metal with a Superconducting Ground State, *Phys. Rev. Lett.* **125**, 247002 (2020).
- [5] B. R. Ortiz, P. M. Sarte, E. M. Kenney, M. J. Graf, S. M. L. Teicher, R. Seshadri, and S. D. Wilson, Superconductivity in the \mathbb{Z}_2 kagome metal KV_3Sb_5 , *Phys. Rev. Mater.* **5**, 034801 (2021).
- [6] Q. Yin, Z. Tu, C. Gong, Y. Fu, S. Yan, and H. Lei, Superconductivity and Normal-State Properties of Kagome Metal RbV_3Sb_5 Single Crystals, *Chinese Physics Letters* **38**, 037403 (2021).
- [7] H. W. S. Arachchige, W. R. Meier, M. Marshall, T. Matsumura, R. Xue, M. A. McGuire, R. P. Hermann, H. Cao, and D. Mandrus, Charge Density Wave in Kagome Lattice Intermetallic ScV_6Sn_6 , *Phys. Rev. Lett.* **129**, 216402 (2022).
- [8] X. Teng, L. Chen, F. Ye, E. Rosenberg, Z. Liu, J.-X. Yin, Y.-X. Jiang, J. S. Oh, M. Z. Hasan, K. J. Neubauer, B. Gao, Y. Xie, M. Hashimoto, D. Lu, C. Jozwiak, *et al.*, Discovery of charge density wave in a kagome lattice antiferromagnet, *Nature* **609**, 490 (2022).
- [9] B. R. Ortiz, L. C. Gomes, J. R. Morey, M. Winiarski, M. Bordelon, J. S. Mangum, I. W. H. Oswald,

- J. A. Rodriguez-Rivera, J. R. Neilson, S. D. Wilson, E. Ertekin, T. M. McQueen, and E. S. Toberer, New kagome prototype materials: discovery of KV_3Sb_5 , RbV_3Sb_5 , and CsV_3Sb_5 , Phys. Rev. Mater. **3**, 094407 (2019).
- [10] Y.-X. Jiang, J.-X. Yin, M. M. Denner, N. Shumiya, B. R. Ortiz, G. Xu, Z. Guguchia, J. He, M. S. Hossain, X. Liu, J. Ruff, L. Kautzsch, S. S. Zhang, G. Chang, I. Belelopolski, *et al.*, Unconventional chiral charge order in kagome superconductor KV_3Sb_5 , Nature Materials **20**, 1353 (2021).
- [11] N. Shumiya, M. S. Hossain, J.-X. Yin, Y.-X. Jiang, B. R. Ortiz, H. Liu, Y. Shi, Q. Yin, H. Lei, S. S. Zhang, G. Chang, Q. Zhang, T. A. Cochran, D. Multer, M. Litskevich, *et al.*, Intrinsic nature of chiral charge order in the kagome superconductor RbV_3Sb_5 , Phys. Rev. B **104**, 035131 (2021).
- [12] C. Mielke, D. Das, J.-X. Yin, H. Liu, R. Gupta, Y.-X. Jiang, M. Medarde, X. Wu, H. C. Lei, J. Chang, P. Dai, Q. Si, H. Miao, R. Thomale, T. Neupert, Y. Shi, R. Khasanov, M. Z. Hasan, H. Luetkens, and Z. Guguchia, Time-reversal symmetry-breaking charge order in a kagome superconductor, Nature **602**, 245 (2022).
- [13] Q. Stahl, D. Chen, T. Ritschel, C. Shekhar, E. Sadrollahi, M. C. Rahn, O. Ivashko, M. v. Zimmermann, C. Felser, and J. Geck, Temperature-driven reorganization of electronic order in CsV_3Sb_5 , Phys. Rev. B **105**, 195136 (2022).
- [14] X. Teng, J. S. Oh, H. Tan, L. Chen, J. Huang, B. Gao, J.-X. Yin, J.-H. Chu, M. Hashimoto, D. Lu, C. Jozwiak, A. Bostwick, E. Rotenberg, G. E. Granroth, B. Yan, *et al.*, Magnetism and charge density wave order in kagome FeGe, Nature Physics **19**, 814 (2023).
- [15] L. Van Hove, The Occurrence of Singularities in the Elastic Frequency Distribution of a Crystal, Phys. Rev. **89**, 1189 (1953).
- [16] M. L. Kiesel, C. Platt, and R. Thomale, Unconventional Fermi Surface Instabilities in the Kagome Hubbard Model, Phys. Rev. Lett. **110**, 126405 (2013).
- [17] M. Kang, S. Fang, J.-K. Kim, B. R. Ortiz, S. H. Ryu, J. Kim, J. Yoo, G. Sangiovanni, D. Di Sante, B.-G. Park, C. Jozwiak, A. Bostwick, E. Rotenberg, E. Kaxiras, S. D. Wilson, J.-H. Park, and R. Comin, Twofold van Hove singularity and origin of charge order in topological kagome superconductor CsV_3Sb_5 , Nature Physics **18**, 301 (2022).
- [18] Y. Hu, X. Wu, B. R. Ortiz, S. Ju, X. Han, J. Ma, N. C. Plumb, M. Radovic, R. Thomale, S. D. Wilson, A. P. Schnyder, and M. Shi, Rich nature of Van Hove singularities in Kagome superconductor CsV_3Sb_5 , Nature Communications **13**, 2220 (2022).
- [19] C. Li, X. Wu, H. Liu, C. Polley, Q. Guo, Y. Wang, X. Han, M. Dendzik, M. H. Berntsen, B. Thiagarajan, Y. Shi, A. P. Schnyder, and O. Tjernberg, Coexistence of two intertwined charge density waves in a kagome system, Phys. Rev. Res. **4**, 033072 (2022).
- [20] H. Tan, Y. Liu, Z. Wang, and B. Yan, Charge Density Waves and Electronic Properties of Superconducting Kagome Metals, Phys. Rev. Lett. **127**, 046401 (2021).
- [21] M. L. Kiesel and R. Thomale, Sublattice interference in the kagome Hubbard model, Phys. Rev. B **86**, 121105 (2012).
- [22] S.-L. Yu and J.-X. Li, Chiral superconducting phase and chiral spin-density-wave phase in a Hubbard model on the kagome lattice, Phys. Rev. B **85**, 144402 (2012).
- [23] W.-S. Wang, Z.-Z. Li, Y.-Y. Xiang, and Q.-H. Wang, Competing electronic orders on kagome lattices at van Hove filling, Phys. Rev. B **87**, 115135 (2013).
- [24] X. Wu, T. Schwemmer, T. Müller, A. Consiglio, G. Sangiovanni, D. Di Sante, Y. Iqbal, W. Hanke, A. P. Schnyder, M. M. Denner, M. H. Fischer, T. Neupert, and R. Thomale, Nature of Unconventional Pairing in the Kagome Superconductors AV_3Sb_5 ($A = K, Rb, Cs$), Phys. Rev. Lett. **127**, 177001 (2021).
- [25] Y.-P. Lin and R. M. Nandkishore, Multidome superconductivity in charge density wave kagome metals, Phys. Rev. B **106**, L060507 (2022).
- [26] R. Tazai, Y. Yamakawa, S. Onari, and H. Kontani, Mechanism of exotic density-wave and beyond-Migdal unconventional superconductivity in kagome metal AV_3Sb_5 ($A = K, Rb, Cs$), Science Advances **8**, eabl4108 (2022).
- [27] A. T. Rømer, S. Bhattacharyya, R. Valentí, M. H. Christensen, and B. M. Andersen, Superconductivity from repulsive interactions on the kagome lattice, Phys. Rev. B **106**, 174514 (2022).
- [28] Y.-M. Wu, R. Thomale, and S. Raghu, Sublattice interference promotes pair density wave order in kagome metals, Phys. Rev. B **108**, L081117 (2023).
- [29] S. C. Holbæk, M. H. Christensen, A. Kreisel, and B. M. Andersen, Unconventional superconductivity protected from disorder on the kagome lattice, Phys. Rev. B **108**, 144508 (2023).
- [30] Y. Dai, A. Kreisel, and B. M. Andersen, Existence of Hebel-Slichter peak in unconventional kagome superconductors, Phys. Rev. B **110**, 144516 (2024).
- [31] H. Li, Y. B. Kim, and H.-Y. Kee, Intertwined Van Hove Singularities as a Mechanism for Loop Current Order in Kagome Metals, Phys. Rev. Lett. **132**, 146501 (2024).
- [32] L. Kautzsch, B. R. Ortiz, K. Mallayya, J. Plumb, G. Pokharel, J. P. C. Ruff, Z. Islam, E.-A. Kim, R. Se-shadri, and S. D. Wilson, Structural evolution of the kagome superconductors AV_3Sb_5 ($A = K, Rb$, and Cs) through charge density wave order, Phys. Rev. Mater. **7**, 024806 (2023).
- [33] V. Scagnoli, L. J. Riddiford, S. W. Huang, Y.-G. Shi, Z. Tu, H. Lei, A. Bombardi, G. Nisbet, and Z. Guguchia, Resonant x-ray diffraction measurements in charge ordered kagome superconductors KV_3Sb_5 and RbV_3Sb_5 , Journal of Physics: Condensed Matter **36**, 185604 (2024).
- [34] R. Khasanov, D. Das, R. Gupta, C. Mielke, M. Elender, Q. Yin, Z. Tu, C. Gong, H. Lei, E. T. Ritz, R. M. Fernandes, T. Birol, Z. Guguchia, and H. Luetkens, Time-reversal symmetry broken by charge order in CsV_3Sb_5 , Phys. Rev. Res. **4**, 023244 (2022).
- [35] Y. Xu, Z. Ni, Y. Liu, B. R. Ortiz, Q. Deng, S. D. Wilson, B. Yan, L. Balents, and L. Wu, Three-state nematicity and magneto-optical Kerr effect in the charge density waves in kagome superconductors, Nature Physics **18**, 1470 (2022).
- [36] C. Guo, C. Putzke, S. Konyzheva, X. Huang, M. Gutierrez-Amigo, I. Errea, D. Chen, M. G. Vergniory, C. Felser, M. H. Fischer, T. Neupert, and P. J. W. Moll, Switchable chiral transport in charge-ordered kagome metal CsV_3Sb_5 , Nature **611**, 461 (2022).
- [37] Y. Xing, S. Bae, E. Ritz, F. Yang, T. Birol, A. N. Capa Salinas, B. R. Ortiz, S. D. Wilson, Z. Wang, R. M. Fernandes, and V. Madhavan, Optical manipulation of the charge-density-wave state in RbV_3Sb_5 , Nature **631**,

- 60 (2024).
- [38] M. H. Christensen, T. Birol, B. M. Andersen, and R. M. Fernandes, Loop currents in AV_3Sb_5 kagome metals: Multipolar and toroidal magnetic orders, *Phys. Rev. B* **106**, 144504 (2022).
- [39] H. Li, H. Zhao, B. R. Ortiz, T. Park, M. Ye, L. Balents, Z. Wang, S. D. Wilson, and I. Zeljkovic, Rotation symmetry breaking in the normal state of a kagome superconductor KV_3Sb_5 , *Nature Physics* **18**, 265 (2022).
- [40] D. R. Saykin, C. Farhang, E. D. Kountz, D. Chen, B. R. Ortiz, C. Shekhar, C. Felser, S. D. Wilson, R. Thomale, J. Xia, and A. Kapitulnik, High Resolution Polar Kerr Effect Studies of CsV_3Sb_5 : Tests for Time-Reversal Symmetry Breaking below the Charge-Order Transition, *Phys. Rev. Lett.* **131**, 016901 (2023).
- [41] C. Farhang, J. Wang, B. R. Ortiz, S. D. Wilson, and J. Xia, Unconventional specular optical rotation in the charge ordered state of Kagome metal CsV_3Sb_5 , *Nature Communications* **14**, 5326 (2023).
- [42] T. Park, M. Ye, and L. Balents, Electronic instabilities of kagome metals: Saddle points and Landau theory, *Phys. Rev. B* **104**, 035142 (2021).
- [43] Y.-P. Lin and R. M. Nandkishore, Complex charge density waves at Van Hove singularity on hexagonal lattices: Haldane-model phase diagram and potential realization in the kagome metals AV_3Sb_5 ($A=K, Rb, Cs$), *Phys. Rev. B* **104**, 045122 (2021).
- [44] M. H. Christensen, T. Birol, B. M. Andersen, and R. M. Fernandes, Theory of the charge density wave in AV_3Sb_5 kagome metals, *Phys. Rev. B* **104**, 214513 (2021).
- [45] H. Zhao, H. Li, B. R. Ortiz, S. M. L. Teicher, T. Park, M. Ye, Z. Wang, L. Balents, S. D. Wilson, and I. Zeljkovic, Cascade of correlated electron states in the kagome superconductor CsV_3Sb_5 , *Nature* **599**, 216 (2021).
- [46] N. Ratcliff, L. Hallett, B. R. Ortiz, S. D. Wilson, and J. W. Harter, Coherent phonon spectroscopy and inter-layer modulation of charge density wave order in the kagome metal CsV_3Sb_5 , *Phys. Rev. Mater.* **5**, L111801 (2021).
- [47] A. Subedi, Hexagonal-to-base-centered-orthorhombic 4Q charge density wave order in kagome metals KV_3Sb_5 , RbV_3Sb_5 , and CsV_3Sb_5 , *Phys. Rev. Mater.* **6**, 015001 (2022).
- [48] M. Gutierrez-Amigo, D. Dangić, C. Guo, C. Felser, P. J. W. Moll, M. G. Vergniory, and I. Errea, Phonon collapse and anharmonic melting of the 3D charge-density wave in kagome metals, *Communications Materials* **5**, 234 (2024).
- [49] E. T. Ritz, R. M. Fernandes, and T. Birol, Impact of Sb degrees of freedom on the charge density wave phase diagram of the kagome metal CsV_3Sb_5 , *Phys. Rev. B* **107**, 205131 (2023).
- [50] J.-X. Yin, Y.-X. Jiang, X. Teng, M. S. Hossain, S. Mardanya, T.-R. Chang, Z. Ye, G. Xu, M. M. Denner, T. Neupert, B. Lienhard, H.-B. Deng, C. Setty, Q. Si, G. Chang, *et al.*, Discovery of Charge Order and Corresponding Edge State in Kagome Magnet FeGe, *Phys. Rev. Lett.* **129**, 166401 (2022).
- [51] S. Wu, M. L. Klemm, J. Shah, E. T. Ritz, C. Duan, X. Teng, B. Gao, F. Ye, M. Matsuda, F. Li, X. Xu, M. Yi, T. Birol, P. Dai, and G. Blumberg, Symmetry Breaking and Ascending in the Magnetic Kagome Metal FeGe, *Phys. Rev. X* **14**, 011043 (2024).
- [52] P. M. Bonetti, Y. Jiang, H. Hu, D. Călugăru, M. M. Scherer, B. A. Bernevig, and L. Classen, Competing phases in kagome magnet FeGe from functional renormalization, *arXiv e-prints*, arXiv:2411.10931 (2024), arXiv:2411.10931 [cond-mat.str-el].
- [53] S. Lee, C. Won, J. Kim, J. Yoo, S. Park, J. Dilling, C. Jozwiak, A. Bostwick, E. Rotenberg, R. Comin, M. Kang, and J.-H. Park, Nature of charge density wave in kagome metal ScV_6Sn_6 , *npj Quantum Materials* **9**, 15 (2024).
- [54] A. Korshunov, H. Hu, D. Subires, Y. Jiang, D. Călugăru, X. Feng, A. Rajapitamahuni, C. Yi, S. Roychowdhury, M. G. Vergniory, J. Strempfer, C. Shekhar, E. Vescovo, D. Chernyshov, A. H. Said, *et al.*, Softening of a flat phonon mode in the kagome ScV_6Sn_6 , *Nature Communications* **14**, 6646 (2023).
- [55] R. Weihrich and I. Anusca, Half Antiperovskites. III. Crystallographic and Electronic Structure Effects in $Sn_{2-x}In_xCo_3S_2$, *Z. Anorg. Allg. Chem.* **632**, 1531 (2006).
- [56] W. Schnelle, A. Leithe-Jasper, H. Rosner, F. M. Schappacher, R. Pöttgen, F. Pielnhofer, and R. Weihrich, Ferromagnetic ordering and half-metallic state of $Sn_2Co_3S_2$ with the shandite-type structure, *Phys. Rev. B* **88**, 144404 (2013).
- [57] Q. Wang, Y. Xu, R. Lou, Z. Liu, M. Li, Y. Huang, D. Shen, H. Weng, S. Wang, and H. Lei, Large intrinsic anomalous Hall effect in half-metallic ferromagnet $Co_3Sn_2S_2$ with magnetic Weyl fermions, *Nature Communications* **9**, 3681 (2018).
- [58] H. Yang, W. You, J. Wang, J. Huang, C. Xi, X. Xu, C. Cao, M. Tian, Z.-A. Xu, J. Dai, and Y. Li, Giant anomalous Nernst effect in the magnetic Weyl semimetal $Co_3Sn_2S_2$, *Phys. Rev. Mater.* **4**, 024202 (2020).
- [59] N. Morali, R. Batabyal, P. K. Nag, E. Liu, Q. Xu, Y. Sun, B. Yan, C. Felser, N. Avraham, and H. Beidenkopf, Fermi-arc diversity on surface terminations of the magnetic Weyl semimetal $Co_3Sn_2S_2$, *Science* **365**, 1286 (2019).
- [60] D. F. Liu, A. J. Liang, E. K. Liu, Q. N. Xu, Y. W. Li, C. Chen, D. Pei, W. J. Shi, S. K. Mo, P. Dudin, T. Kim, C. Cacho, G. Li, Y. Sun, L. X. Yang, Z. K. Liu, S. S. P. Parkin, C. Felser, and Y. L. Chen, Magnetic weyl semimetal phase in a kagomé crystal, *Science* **365**, 1282 (2019).
- [61] Y. Okamura, S. Minami, Y. Kato, Y. Fujishiro, Y. Kaneko, J. Ikeda, J. Muramoto, R. Kaneko, K. Ueda, V. Kocsis, N. Kanazawa, Y. Taguchi, T. Koretsune, K. Fujiwara, A. Tsukazaki, R. Arita, Y. Tokura, and Y. Takahashi, Giant magneto-optical responses in magnetic Weyl semimetal $Co_3Sn_2S_2$, *Nature Communications* **11**, 4619 (2020).
- [62] F. Pielnhofer, J. Rothbäller, P. Peter, W. Yan, F. M. Schappacher, R. Pöttgen, and R. Weihrich, Half antiperovskites vi: On the substitution effects in shandites $insn_2-co_3s_2$, *Zeitschrift für anorganische und allgemeine Chemie* **640**, 286 (2014).
- [63] J. Corps, P. Vaqueiro, A. Aziz, R. Grau-Crespo, W. Kockelmann, J.-C. Jumas, and A. V. Powell, Interplay of Metal-Atom Ordering, Fermi Level Tuning, and Thermoelectric Properties in Cobalt Shandites $Co_3M_2S_2$ ($M = Sn, In$), *Chemistry of Materials* **27**, 3946 (2015).
- [64] R. Weihrich, A. C. Stückl, M. Zabel, and W. Schnelle, Magnetischer Phasenübergang des $Co_3Sn_2S_2$, *Zeitschrift für anorganische und allgemeine Chemie* **630**, 1767

- (2004).
- [65] T. Zhang, T. Yilmaz, E. Vescovo, H. X. Li, R. G. Moore, H. N. Lee, H. Miao, S. Murakami, and M. A. McGuire, Endless Dirac nodal lines in kagome-metal $\text{Ni}_3\text{In}_2\text{S}_2$, npj Computational Materials **8**, 155 (2022).
- [66] M. R. Norman, Colloquium: Herbertsmithite and the search for the quantum spin liquid, Rev. Mod. Phys. **88**, 041002 (2016).
- [67] N. Hänni, M. Frontzek, J. Hauser, D. Cheptiakov, and K. Krämer, Low Temperature Phases of $\text{Na}_2\text{Ti}_3\text{Cl}_8$ Revisited, Zeitschrift für anorganische und allgemeine Chemie **643**, 2063 (2017).
- [68] A. Paul, C.-M. Chung, T. Birol, and H. J. Changlani, Spin-lattice Coupling and the Emergence of the Trimerized Phase in the $S = 1$ Kagome Antiferromagnet $\text{Na}_2\text{Ti}_3\text{Cl}_8$, Phys. Rev. Lett. **124**, 167203 (2020).
- [69] C. Bradley and A. Cracknell, *The Mathematical Theory of Symmetry in Solids: Representation Theory for Point Groups and Space Groups*, EBSCO ebook academic collection (OUP Oxford, 2010).
- [70] D. M. Hatch and H. T. Stokes, INVARIANTS: program for obtaining a list of invariant polynomials of the order-parameter components associated with irreducible representations of a space group, Journal of Applied Crystallography **36**, 951 (2003).
- [71] H. T. Stokes, D. M. Hatch, and B. J. Campbell, INVARIANTS, ISOTROPY Software Suite, iso.byu.edu.
- [72] J. Wilson and A. Yoffe, The transition metal dichalcogenides discussion and interpretation of the observed optical, electrical and structural properties, Advances in Physics **18**, 193 (1969).
- [73] X. Gonze, B. Amadon, G. Antonius, F. Arnardi, L. Baguet, J.-M. Beuken, J. Bieder, F. Bottin, J. Bouchet, E. Bousquet, N. Brouwer, F. Bruneval, G. Brunin, T. Cavignac, J.-B. Charraud, *et al.*, The Abinit project: Impact, environment and recent developments, Comput. Phys. Commun. **248**, 107042 (2020).
- [74] A. H. Romero, D. C. Allan, B. Amadon, G. Antonius, T. Applencourt, L. Baguet, J. Bieder, F. Bottin, J. Bouchet, E. Bousquet, F. Bruneval, G. Brunin, D. Caliste, M. Côté, J. Denier, *et al.*, ABINIT: Overview, and focus on selected capabilities, J. Chem. Phys. **152**, 124102 (2020).
- [75] X. Gonze and C. Lee, Dynamical matrices, Born effective charges, dielectric permittivity tensors, and interatomic force constants from density-functional perturbation theory, Phys. Rev. B **55**, 10355 (1997).
- [76] J. P. Perdew, A. Ruzsinszky, G. I. Csonka, O. A. Vydrov, G. E. Scuseria, L. A. Constantin, X. Zhou, and K. Burke, Restoring the Density-Gradient Expansion for Exchange in Solids and Surfaces, Phys. Rev. Lett. **100**, 136406 (2008).
- [77] F. Jollet, M. Torrent, and N. Holzwarth, Generation of projector augmented-wave atomic data: A 71 element validated table in the xml format, Computer Physics Communications **185**, 1246 (2014).
- [78] M. Torrent, F. Jollet, F. Bottin, G. Zérah, and X. Gonze, Implementation of the projector augmented-wave method in the ABINIT code: Application to the study of iron under pressure, Computational Materials Science **42**, 337 (2008).
- [79] M. van Setten, M. Giantomassi, E. Bousquet, M. Verstraete, D. Hamann, X. Gonze, and G.-M. Rignanese, The pseudodojo: Training and grading a 85 element optimized norm-conserving pseudopotential table, Computer Physics Communications **226**, 39 (2018).
- [80] P. Gütlich, K.-J. Range, C. Felser, C. Schultz-Münzenberg, W. Tremel, D. Walcher, and M. Waldeck, The Valence States of Nickel, Tin, and Sulfur in the Ternary Chalcogenide $\text{Ni}_3\text{Sn}_2\text{S}_2$ - XPS, ^{61}Ni and ^{119}Sn Mössbauer Investigations, and Band Structure Calculations, Angewandte Chemie International Edition **38**, 2381 (1999).
- [81] A. Aziz, P. Mangelis, P. Vaqueiro, A. V. Powell, and R. Grau-Crespo, Electron and phonon transport in shandite-structured $\text{Ni}_3\text{Sn}_2\text{S}_2$, Phys. Rev. B **94**, 165131 (2016).
- [82] Y. Yanagi, J. Ikeda, K. Fujiwara, K. Nomura, A. Tsukazaki, and M.-T. Suzuki, First-principles investigation of magnetic and transport properties in hole-doped shandite compounds $\text{Co}_3\text{In}_x\text{Sn}_{2-x}\text{S}_2$, Phys. Rev. B **103**, 205112 (2021).
- [83] L. Elcoro, B. Bradlyn, Z. Wang, M. G. Vergniory, J. Cano, C. Felser, B. A. Bernevig, D. Orobengoa, G. d. I. Flor, and M. I. Aroyo, Double crystallographic groups and their representations on the Bilbao Crystallographic Server, J. Appl. Crystallogr. **50**, 1457 (2017).